3 X-ray Beam Lines

3.1 Introduction

The unprecedented characteristics of the electron beam produced by an ERL will enable the development of entirely new generations of novel hard x-ray insertion devices, x-ray optics, and end-station instrumentation which will push back the research frontiers for diverse research fields including advanced materials, nanoscale, non-periodic, non-equilibrium, and transient structures. The ERL produces a low emittance, round, $5\,\mathrm{GeV}$, $100\,\mathrm{mA}$ electron beam in the form of picosecond pulses at $1.3\,\mathrm{GHz}$. Using insertion devices this exquisite electron beam can produce nearly diffraction-limited hard x-ray beams with fluxes surpassing those available at current third-generation synchrotron hard x-ray beamlines.

This section on x-rays is a conceptual design document. It is not a science case. It is not a technical design document. Nor does this section attempt to be comprehensive. Rather, the goal is to explore some of the spectacular scientific opportunities an ERL-based hard x-ray source might enable. Since the current generation of high-spectral brightness hard x-ray machines (e.g., NSLS-II and PETRA-III) has large research and development efforts addressing many of the technical challenges an ERL-based hard x-ray facility will face, we can expect significant advances in hard x-ray optics and instrumentation optimized for intense, spatially coherent sources in the next few years with a high degree of confidence. Construction of an ERL facility will follow these sources. The x-ray beamline technology available will build on this foundation, benefiting enormously from the community's experience and expertise. Therefore, we concentrate here on describing new opportunities only possible with ERL quality beams.

We envision that the choice, specification, design, construction, and operation of x-ray beamlines at the ERL facility will be performed by a community process. Modeled on Cornell's very successful experience with both the G-line facility and the CLEO collaboration, researchers from around the world will be encouraged to become 'PIs' and base their frontier x-ray based research programs at Cornell's ERL. These research programs will optimize beamlines for specific types of measurements and research. Their facilities and expertise will then attract a diverse community of users to the facility. This will begin with a community-based process to select the most promising research opportunities, then the preparation of a detailed initial scientific program, and then the design of the specific capabilities. The design of the experimental stations will vary depending on the scientific target; provisions must be made to enable the incorporation of biohazards, hazardous gases and materials, nanofabrication tools, electron microscopes, materials deposition systems, laser systems for optical tweezers, coherent control of molecules, and pump-probe applications in the experimental floor.

The material below is organized into the following sections:

- **Novel x-ray optics enabled by ERL:** The small size and energy spread of the ERL's electron beam will enable new types of novel insertion devices. These will be briefly

reviewed in this section and are explored in detail in the accelerator physics section.

- **X-ray beamline standard components:** Many of the components will be common to all the x-ray beamlines. These components are identified and their requirements specified. These standard components form the foundation for the x-ray beamline cost estimates.

- **High coherent flux beamline for diffractive imaging and dynamics:** With its quasi-continuous flux of coherent hard x-ray beams, the ERL will provide unprecedented capabilities for coherence-based structural studies of both crystalline and nonperiodic samples. The coherent flux density will be comparable to the total flux densities at third-generation sources. The quasi-continuous time structure will enable new opportunities in studies of time evolution of non-equilibrium systems, extending the achievable range of resolution to shorter time- and length-scales and bridging the $10^{-9} - 10^{-3}$ s timescale gap between free electron laser ($10^{-12} - 10^{-9}$ s) and storage ring sources ($> 10^{-3}$ s).

- **Nanobeam small- and wide-angle scattering beamline:** In scattering experiments with x-ray microbeams, two seemingly contradictory requirements need to be reconciled: the smallest possible spot size for optimum real-space resolution and the lowest possible angular divergence for high-reciprocal space resolution. The nearly diffraction-limited x-ray beams of the ERL thus are sensitive to all length scales from atomic to macroscopic and are ideally suited for the study of hierarchical structures found in soft condensed matter.

- **Short pulse beamline:** The picosecond pulses of the ERL are well matched to the characteristic time scale for atomic motions. Additional bunch compression and the flexible pulse train structure of the ERL further enable new studies utilizing lasers for optical control of the sample. X-ray scattering will be the dominant tool for probing laser-induced changes in atomic positions, while x-ray absorption and emission spectroscopy will be used to probe changes in the electronic structure.

- **High resolution inelastic scattering:** To be broadly applicable, energy-resolved scattering techniques require unprecedented average spectral flux and brightness. The new designs of long insertion devices enabled by the ERL produce the necessary x-ray beams with reduced power on x-ray optics. IXS is sensitive to the dynamical properties of materials at time scales ranging from 10^{-16} to 10^{-11} seconds at atomic to mesoscopic length scales. Systems of interest include electron density fluctuations, inner-shell electronic excitations, collective vibrations, and electron momentum density.

- **Nanofocus beamline:** The wide application of x-rays to nanoscale science is heavily dependent on the availability of 1 to 10 nm diameter x-ray beams with useful flux, angular divergence, and energy resolution. Storage ring sources will be able to work on the threshold of this area, but the small round ERL source size will generate as many x-rays onto a square nanometer of a sample as many third-generation source beamlines can focus onto a square micron.

3.2 Novel insertion device operation modes

The electron beam in an ERL has unique characteristics that enable the production of x-ray beams with properties qualitatively different from those possible from storage rings. For example, by employing damping wigglers and low-emittance growth electron optics, the current generation of storage rings (e.g., NSLS-II and PETRA-3) create nearly diffraction-limited hard x-ray sources in the vertical plane (but not in the horizontal plane). While these sources will be "nearly at the ultimate limit of storage-ring light sources set by the intrinsic properties of the synchrotron radiation process,"[1] their performance is still limited by storage-ring physics. The ERL goes beyond fundamental storage-ring limits in several respects. First, the energy spread of the ERL is aproximately five times smaller, enabling more effective use of long undulators, increasing both the spectral brightness and the power of the x-ray beam. The ERL does not require an injection orbit, enabling undulators with small horizontal gaps, creating the possibility of horizontal diffraction planes. Furthermore, the ERL's transverse emittances are equal, enabling circular gaps, and truly helical insertion devices and full transverse coherence in both the horizontal and vertical planes. Finally, the ERL does not require a periodic magnetic lattice, enabling an electron beam to be independently optimized for each insertion device. Each of these is discussed in turn below.

3.2.1 Long undulators

When the angular divergence of the electron beam is smaller than the radiation cone of a single electron (diffraction limit), the spectral width of an undulator peak is given by

$$\frac{\Delta\lambda}{\lambda} \simeq \sqrt{\left(\frac{1}{N}\right)^2 + \left(\frac{\Delta E}{E}\right)^2}, \tag{3.2.1}$$

where $\Delta E/E$ is the energy spread of the electron beam and N is the number of poles. This relationship limits the maximum useful length of an undulator. Since the spectral brightness scales as N^2 , increasing the number of poles can significantly increase the spectral brightness holding all other electron beam parameters constant. In the ERL, $\Delta E/E = 2 \times 10^{-4}$, which implies $N = 5000$. We therefore propose to develop long undulators with thousands of poles.

3.2.2 Novel insertion devices

The small, round electron beams of an ERL support several innovative insertion device (ID) designs that both enhance performance and reduce complexity and cost. We propose to develop two different types of novel insertion devices that take advantage of the round ERL beam. The first is a pure permanent magnet (PPM) undulator. The second novel design is the superconducting bifilar wound double helix ID (scID). Both take advantage of the small energy spread and both can operate as helical undulators.

Helical undulators

Helical undulators have several very useful properties. Only the first harmonic is present on-axis, opening the possibility of optics-less monochromatic beamlines. Circularly polarized

radiation behaves like unpolarized radiation in conventional scattering experiments that do not involve magnetic materials or chiral molecules. Analysis of experiments that involve scattering in an arbitrary plane (e.g. crystallography) is simplified with circular radiation since no polarization correction is needed. Finally, the power density in the beam for the same current or magnetic field strength is greater because the magnetic field never goes to zero.

Delta undulator

The small round electron beam enables PPM geometries that generate magnetic field strengths limited only by the critical field of the material. At the same time, both the amount of magnetic material required and the field energy stored can be dramatically reduced. The reduction in magnetic material significantly lowers the cost of the insertion device. The lower-stored energy reduces the forces on the structure with concomitant reductions in both mechanical complexity and cost. The polarization of the resulting x-ray beam can be changed between horizontal, vertical or helical simply by shifting the magnet arrays. The 'Delta' design is discussed in detail in §2.7.3.

Superconducting helical undulator

Helical undulators have only the first harmonic in forward direction. A simple collimator thus becomes a monochromator. The energy bandwidth is given by 1 over the number of poles of the undulator. This provides an elegant way to deliver coherent hard x-ray beams into experimental stations.

3.2.3 Beamline specific control of the electron beam

From an electron optics viewpoint, the ERL is more like a linear accelerator than a storage ring. In particular, there is no significant benefit from imposing the constraint of a periodic lattice. Thus, the electron optics can be optimized independently for each insertion device. That is, the beta function can be specified independently for each insertion device. Indeed, it can be altered for a given device without affecting the other insertion devices! Instead of being able to offer a fixed set of low- and high-beta straight sections, the ERL supports a significant range of beta functions at each insertion device, and these choices can be altered without significantly impacting the rest of the ERL. This degree of freedom significantly enhances the ability of insertion device designers to optimize the x-ray source for particular applications.

3.2.4 Electron beam focusing of x-rays

The electron beam waist (beta function minimum) can be positioned at locations other than the center of an insertion device. When the electron divergence dominates over the radiative divergence, this can be used to move the virtual location of the x-ray source either upstream or downstream of the ID, e.g. to focus x-ray beams onto a sample without additional x-ray optics. In the ERL, where electron beams are diffraction limited, the electron-beam divergence does not dominate, but moving the virtual source point may still help to optimize beam properties at a collimator or to compensate for the energy dependence of the focal length of refractive or

diffractive lenses. The ERL can take advantage of these options because of its flexible electron optics.

3.2.5 Horizontal diffraction plane

Either circularly or vertically polarized x-ray beams enable the use of a horizontal diffraction plane. A horizontal diffraction plane is of tremendous advantage (relative to vertical, as is typical for present-day storage ring sources) for building large diffractometers. This is especially true either for heavy objects or for cases where positioning or angular stability must be maintained over a large range of scattering angles.

3.2.6 Optics-free beamlines

Preserving the exquisite brilliance and coherence of ERL x-ray beams will pose major challenges to x-ray optics development, in particular for wavefront-preserving mirrors, monochromators, and windows. For a variety of applications, however, the beam generated by an ERL undulator has already the required properties.

- A 20 mm period undulator will radiate coherently over a length of 5 m, as given by the small longitudinal energy spread of the ERL electron beam. Hence such an undulator would generate x-ray beams at the theoretical limit of undulator radiation, i.e. at a bandwidth of 0.4%. At CHESS there is a rich experience of using multilayer monochromators yielding x-ray beams with bandwidths of 0.3% to 2%, and many non-resonant scattering experiments would work ideally at this bandwidth.

- Harmonic-rejection mirrors would not be needed for either low-K planar undulators or helical undulators. Planar undulators with $K < 0.3$ emit 99% of their radiation in the forward cone into the first harmonic. In helical undulators higher harmonics are suppressed.

- Using windowless, differentially pumped front-ends will eliminate wave-front distortion at windows and filters. Vacuum-technology for beamlines is well-developed in the soft x-ray range. With a series of differential pumping stages close to the sample beams can be brought out into ambient environment or will be directly connected to sample vacuum systems.

- ERL x-ray beams have such small size and divergence that an undulator beam would spread out no larger than 0.5 mm at 50 m from the source. Hence prefocusing is not needed

Use of such an optics-free mode would lead to a paradigm shift in x-ray optics, where the effort would now be spent on perfecting the source (electron beam, undulator) rather than trying to further improve conventional x-ray optics, where roughness and slope error are already close to principal limits.

References

[1] *NSLS-II Preliminary Design Report.* Technical report, Brookhaven National Laboratory (2007). http://www.bnl.gov/nsls2/project/PDR/.

3.3 X-ray beamline standard components

As stated in the introduction to this section, the design of x-ray beamlines and experimental stations will follow, and benefit from, years of research and developent now ongoing at the current generation of high spectral brightness hard x-ray machines (e.g., NSLS-II and PETRA-III). The x-ray beam line technology available will build on this foundation, benefiting enormously from the community's experience and expertise. The ERL x-ray beamlines will share some, and push other, requirements for coherence preservation and stability. One particular design consideration will be that some beamlines may choose to avoid using optical elements like monochromators to select wavelengths, instead matching the insertion device and experimental data collection strategy to make use of the full energy bandwidth of undulator harmonics. Because such considerations are early in the planning stages, in addition to the large community research and developent efforts at other sources mentioned above, this section will only go so far as to identify the engineering challenges and benefits (efficiencies) we foresee for creating standard beamline components.

3.3.1 Machine to x-ray beamline transitions and primary x-ray beamstops

An integral part of the vacuum containment vessel, the upstream-most parts of the x-ray beamlines on the ERL must also dissipate any synchrotron radiation from dipole magnets (a masking function) and provide the fastest possible early warning of steering excursions of the insertion device beams. Excursion protection is needed in light sources even today because the upstream-most components – crotches, copper-flared chambers, and apertures – are sufficiently close to the radiation sources that they cannot withstand direct strikes of high power density x-ray beams for sizable periods of time. Providing fast excursion signals will likely involve fast x-ray beam position monitors (BPMs) integral to the copper-flared chamber. (Other solutions involving temperature sensing or residual gas generation might not prove fast enough.) This fast detector needs to be upstream of the primary and secondary x-ray beamstops so that machine tuning and alignment can be done before full commissioning of x-ray beamlines. During normal operations such excursion monitors may play a role in equipment protection, ensuring that x-ray beams are centered before allowing the primary and secondary beamstops to open.

Vacuum gate valves will surround the primary and secondary x-ray beamstops. These sector valves protect the critically clean, ultra-high vacuum environment of the ERL. At least one of the gate valves along the x-ray beamlines will be fast, able to close in millisecond timeframes and accept trigger signals from downstream monitors that sense vacuum difficulties or other possible contaminant sources.

Though it is too early to elaborate on design here, a significant engineering, controls and safety effort will be needed to create the 'ready chain' interlock system that would enable gate valve opening, x-ray beamstop opening, etc. Each of the components along the x-ray beamline mentioned below would need to provide sensors and operational status signals that populate the 'ready chain' interlock system.

3.3.2 Apertures and secondary x-ray BPM

The x-ray beamlines require critical apertures and x-ray BPMs that serve two functions; x-ray beam containment and shaping, and position and stability diagnostics and feedback. Apertures and beamline vacuum design can provide differential pumping that may prove critically important to separate downstream gas loads from contaminating accelerator and insertion device chambers.

3.3.3 Upstream x-ray optics

Some of the x-ray beamlines might need upstream optical components such as apertures, white beam mirrors, pulse arrival detectors or pulse shaping or synchronization devices, x-ray focusing elements (i.e. Fresnel zone plates), or other unforeseen experimental apparatus. We expect, then, to design x-ray drift spaces upstream of the shielding ratchet wall that permit equipment installations. At this conceptual stage, these spaces are located at the half-way between the source point and the sample position. Some of the items, e.g., white beam mirrors, may require substantial amounts of research and developent to achieve the performance needed by an ERL source. Others, e.g., schemes to measure pulse arrival, will gain enormously by ongoing research efforts at existing third and fourth-generation sources.

3.3.4 Ratchet wall

The shielding 'ratchet wall' separates the accelerator tunnel from the x-ray experimental areas. This shield wall requires critical engineering of shutters, located on the accelerator side of the wall, whose function is to complete the radiation shielding of the wall system. This mates to an x-ray transport pipe through a heavy concrete wall (in general), followed by the upstream-most window section of the x-ray optics enclosure. The shutter, wall and window design provides yet another opportunity to build differential pumping and vacuum isolation into the beamline. The design of windows will be a critical part of delivering fully coherent x-ray beams to experiments. In many cases the best window design might involve no window at all, but rather providing vacuum transitions between the accelerator and x-ray optics sections (if used). This project will involve exploring vacuum isolation solutions that involve no hard materials, using instead plasma containment [1] in addition to the more standard method of differential pumping.

3.3.5 X-ray monochromator and beam shaping systems

Critically important to the success of any experiment is the conditioning of the x-ray beam in terms of energy spread, wavelength, size, angular divergence, and timing. Many of these attributes are tightly coupled. Standard designs will be needed for white-beam apertures and slit systems, monochromatic and wide-energy bandpass optics (focusing and non-focussing), monochromatic mirrors, monochromatic apertures and slits, and x-ray beam viewers and diagnostic tools. The design of any apparatus to make these parameters adjustable requires careful consideration of (1) high-heat-load and high-power-density capable optics, apertures, etc., (2) brilliance preserving optics, filters, etc., that provide or maintain high transverse coherence, and (3) optics used to manipulate, preserve and/or produce short x-ray pulses
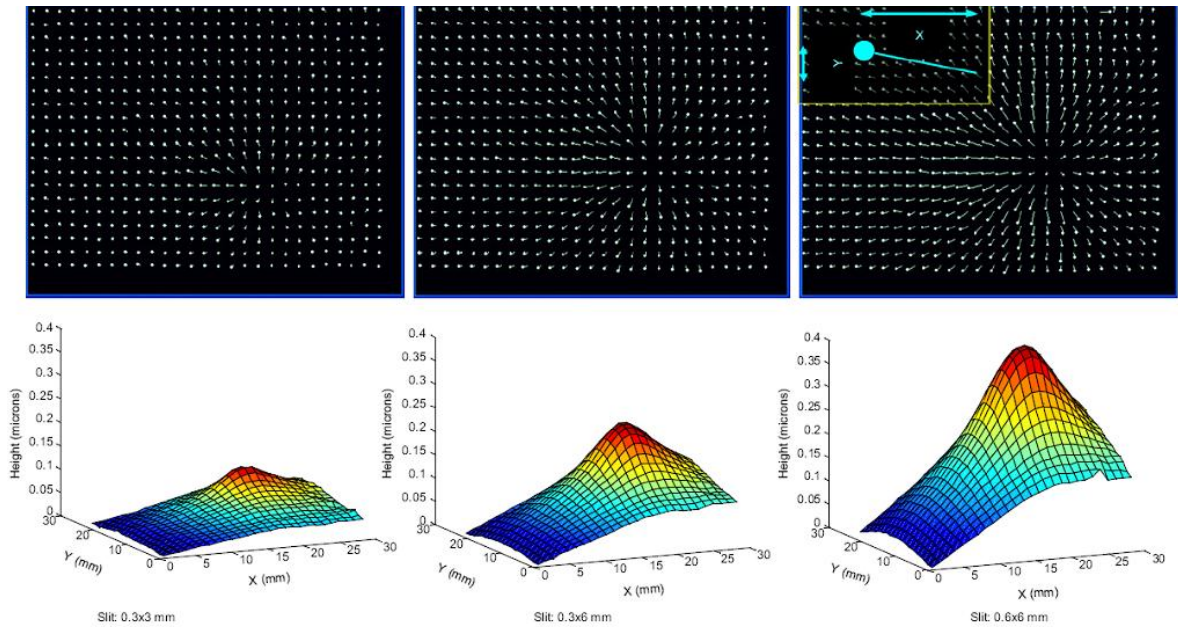
Figure 3.3.1: Study of x-ray beam heat-loading distortion of a silicon crystal tilted 5 degrees, for three different slit openings. On top, the dot patterns recorded by the video camera; the length of the line indicates the displacement of the dot versus no x-ray beam. Below, the reconstructed crystal surface profiles show displacements up to 400 nm.

and critical synchronization. In each of these areas there is a rich history of research and development solutions [2–4] and many ongoing efforts aimed at delivering state-of-the-art performance from current and future sources.

An example of one of the types of studies which will be needed is the direct measurement of the localized thermal expansion of the monochromator due to heating by the x-ray beam as shown in Fig. 3.3.1. In addition to degrading the energy resolution and angular collimation of the resulting beam, these monochromator distortions introduce optical pathlength differences which degrade the plane wave nature of the coherent x-ray beam.

3.3.6 Optics enclosures and experimental room design

Design of x-ray optical enclosures involves civil engineering, radiation containment and experimental performance considerations. X-ray beam shutters will follow similar research and development to those serving upstream, either containing white beam, filtered white beam, or monochromatic beam. Bremsstrahlung shielding design will be essential. Heating, Venting, and Air-Conditioning (HVAC) design is necessary to provide the environmental stability needed. Mechanical and civil engineering design is essential to provide the short and long term stability needed for micro- and nanobeam experiments.

References

[1] Pinkoski, B. T., *et al. X-ray transmission through a plasma window.* Review of Scientific Instruments, **72** (Copyright 2001, IEEE), pages 1677–9 (2001).

[2] Revesz, P., A. Kazimirov, and I. Bazarov. *In situ visualization of thermal distortions of synchrotron radiation optics.* Nuclear Instruments & Methods in Physics Research, Section A (Accelerators, Spectrometers, Detectors and Associated Equipment), **576** (Copyright 2007, The Institution of Engineering and Technology), pages 422–9 (2007).

[3] Revesz, P., A. Kazimirov, and I. Bazarov. *Optical measurement of thermal deformation of multilayer optics under synchrotron radiation.* Nuclear Instruments and Methods in Physics Research Section A: Accelerators, Spectrometers, Detectors and Associated Equipment, **582** (1), pages 142–145 (2007).

[4] Shen, Q. *et al. Present and Future Optics Challenges at CHESS and for Proposed Energy Recovery Linac Source of Synchrtron Radiation.* SPIE, **4501** (2001).

3.4 Flexible high spectral brightness beamline for diffractive imaging and dynamics

3.4.1 Overview

The high spectral-brightness beamline at the Cornell ERL will be the source of the world's highest quasi-continuous flux of coherent, hard x-ray beams (see Table 3.4.1). The *coherent* flux density at the ERL is expected to be comparable with the *total* flux densities at many third-generation sources. It will provide unprecedented capabilities for coherence-based structural studies of both crystalline and noncrystalline samples. Supported imaging techniques will include coherent x-ray scattering, coherent diffractive imaging, and Fresnel coherent imaging, as well as ptychography-based techniques in order to image extended objects.

The exceptionally high coherent flux and quasi-continuous time structure will enable new opportunities in studies of time evolution of non-equilibrium systems, extending the achievable range of resolution to shorter time and length scales. The high-average-brilliance, high-repetition-rate beams at the ERL will bridge the $10^{-9} - 10^{-3}\,$s gap between timescales obtainable at high-peak-brilliance, low-repetition-rate sources like the free electron laser $(10^{-12} - 10^{-9}\,$s$)$ and lower-brilliance, high-repetition-rate third generation sources ($> 10^{-3}\,$s$)$.

The proposed 25-meter Delta undulator will produce a remarkably well collimated and monochromatic x-ray beam, even without optics ($8.5\,\mu$rad FWHM in both directions at $8\,$keV, 0.2% FWHM bandwidth). The flexible Delta design will allow unprecedented control over the polarization. The fact that the ERL is not a storage ring presents opportunities such as the ability to tune the electron-beam transport optics to optimize the source for each particular application. The beamline and the optics will therefore be designed for flexibility, to allow various modes of operation, including optics-less and high-energy modes, with an eye towards exploring new capabilities and techniques that may be enabled by this unique source of hard X-rays.

3.4.2 State of the art

This state-of-the-art beamline is projected to be the most brilliant quasi-continuous source of X-rays in the world. Realizing this goal will require us to draw on the ongoing pioneering work done at third-generation sources, both in terms of instrumentation and technique development. The beamline will benefit from research and development that is currently underway to meet the optics and instrumentation requirements of recently-upgraded facilities like PETRA-III and new facilities like NSLS-II. For example, we will require optical elements that minimize distortions to the coherent wavefront.

Table 3.4.1: Comparison of key properties (spectral brightness, coherent fraction, etc.) for various sources. Anticipated properties are listed in the case of NSLS-II and the ERL.

Electron Source	APS	ESRF	Spring-8	NSLS-II	ERL High Coherence[1]	ERL High Flux[1]
Energy(GeV)	7.0	6.03	8.0	3.0	5.0	5.0
$\Delta E/E(\%)$	0.096	0.11	0.11	0.099	0.0088	0.019
Current(mA)	100	200	100	500	25	100
ϵ_N (nm rad)[2]	2.5	4.025	3.4	0.508	0.0236	0.0557
Coupling	0.00969	0.006	0.002	0.016	0.815	0.807
ϵ_x/ϵ_y (nm rad)	2.49/0.024	4.0/0.024	3.39/0.007	0.5/0.008	0.013/0.011	0.031/0.025
β_x/β_y(m)	14.4 / 4	0.5 /2.73	21.7/14.1	2.02/1.06	3.98/3.98	3.98/3.98
α_x/α_y	0 / 0	0 / 0	0 / 0	0 / 0	0 / 0	0 / 0
η_x/η_y(m)	0.124 / 0	0.037 / 0	0.103 / 0	0 / 0	0 / 0	0 / 0
η_x'/η_y'	0 / 0	0 / 0	0 / 0	0 / 0	0 / 0	0 / 0
σ_x/σ_y (μm)	224 / 9.82	60.5 / 8.10	294 / 9.78	31.8 / 2.91	7.19 / 6.49	11.1 / 9.95
σ_x'/σ_y' (μrad)	13.2 / 2.46	89.5 / 2.97	12.5 / 0.69	15.7 / 2.75	1.81 / 1.63	2.78 / 2.50
Undulator / X-ray Source	Undulator A	In vacuum undulator	In vacuum undulator	U20 undulator	Helical Delta	Helical Delta
Beamline	8ID	ID27	BL19XU	Projected	Projected	Projected
Length(m)	2.4	4	25	3	25	25
Period(mm)	33	23	32	20	19	19
Min. Gap(mm)	10.5	6	12	5	5	5
B_{max} (T)	0.891	0.75	0.59	0.97	0.85	0.85
K_{max}	2.74	1.61	1.76	1.81	1.43	1.43
Σ_x/Σ_y (μm)	224 / 10.1	60.5 / 8.56	294.1 /12.0	32.1 / 5.11	10.0 / 9.55	13.1 / 12.1
Σ_x'/Σ_y' (μrad)[3]	14.3 / 6.21	89.6 / 5.31	12.6 / 1.89	18.0 / 9.21	2.52 / 2.40	3.29 / 3.05
Spectral Brightness[3,4]	4.2×10^{19}	1.6×10^{20}	6.4×10^{20}	8.9×10^{20}	7.37×10^{22}	1.1×10^{23}
Coherent Fraction (%)[3]	0.080	0.054	0.085	0.82	23	7.6
Coherent Flux (ph/s/0.1%)[3,4]	2.5×10^{11}	9.5×10^{11}	3.9×10^{12}	5.4×10^{12}	4.0×10^{14}	5.3×10^{14}

(1) Projected; (2) SPECTRA-8.0.10 calculates ϵ_x and ϵ_y based on a 'Natural Emittance' parameter ϵ_N and the coupling constant. When comparing an isotropic source like the ERL with existing sources, ϵ_x and ϵ_y are the relevant parameters, not ϵ_N; (3) Values at 8 keV;(4) Spectral brightness reported in standard units of ph/s/mm^2/mrad^2/0.1%.

Researchers are currently developing metrology techniques to investigate such distortions in mirrors, monochromators and other optical elements [1]. Researchers have also recently made progress towards fabricating X-ray mirrors with the stringent tolerances required by nanofocus and coherent scattering beamlines, such as in-situ surface figure determination and correction [2] and adaptive wavefront corrections [3]. The projected performance of this beamline will be possible as a result of the efforts of the larger community.

3.4.3   Example experiments

Coherent imaging of biological samples
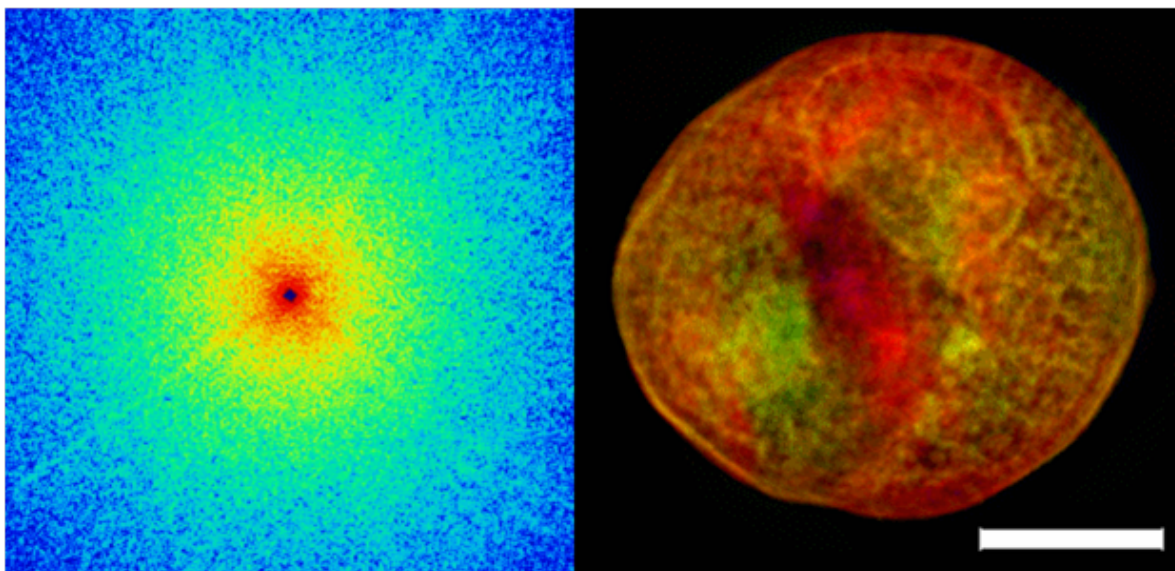
Figure 3.4.1: Coherent scattering image (left) and real-space reconstruction of a freeze-dried yeast cell to 30 nm resolution (right) [4].

X-ray diffraction microscopy, where a sample is illuminated with a coherent source of X-rays and the resulting continuous scattering pattern is algorithmically inverted to yield real-space structural information, is currently of great interest for studies of biological samples. For example, in Fig. 3.4.1, the coherent scattering pattern and resulting structural solution with 30 nm resolution is illustrated for a freeze-dried yeast cell [4]. Groups have recently begun to use x-ray diffraction microscopy to image biological samples in the frozen hydrated state [6]. The resolution that can be obtained in such measurements is limited by the degree of contrast between protein and vitreous ice, and by the onset of radiation damage, which for 3D reconstructions is predicted to be 10 nm without the introduction of contrast-enhancing agents [7].

Coherent imaging of frozen-hydrated biological samples is challenging due to the formation of ice around the sample during long exposures, and to the dynamical scattering effects that arise with softer x-rays. Recently, 30 nm resolution was reported for diffraction microscopy of frozen hydrated samples using 8 keV x-rays.[6] The ERL high coherent flux beamline will
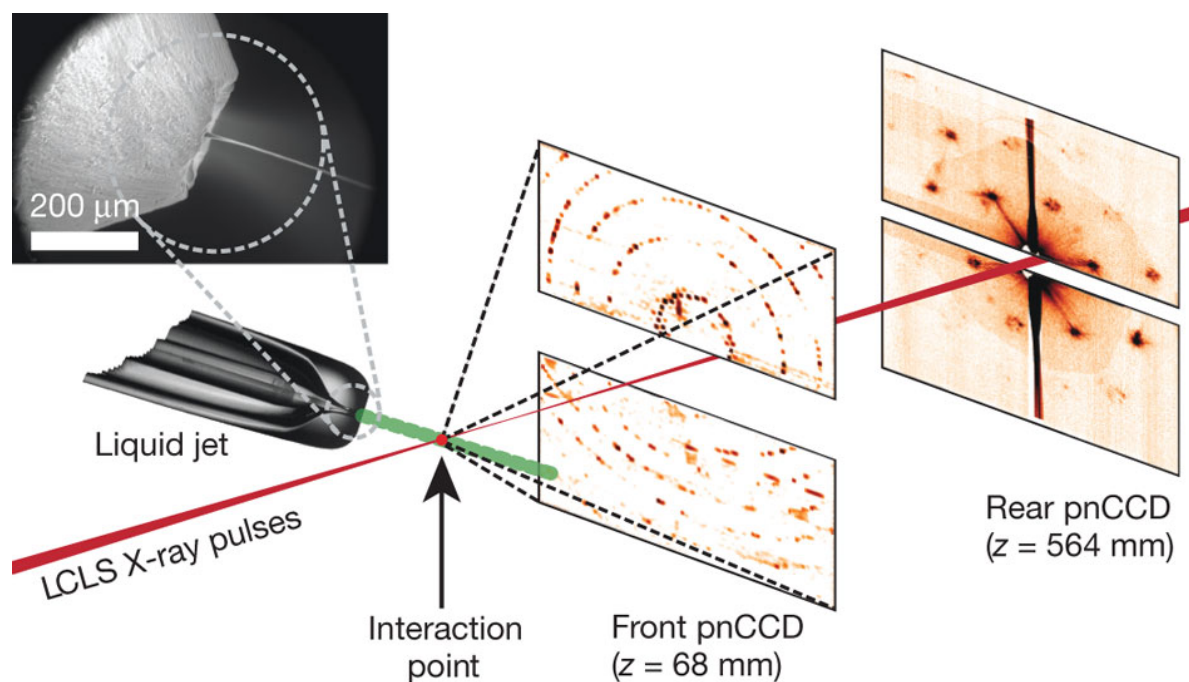
Figure 3.4.2: Illustration of the serial crystallography method, reproduced from [5]

offer high brilliance in x-rays down to $4\,\mathrm{keV}$ for imaging of frozen hydrated biological samples, decreasing integration times to reduce the effects of ice buildup and decreasing the effects of dynamical scattering that occur with soft/ x-rays.

Serial crystallography: beating radiation damage

One exciting application of this high brilliance beamline is the ability to determine the structure of non-crystalline or nanocrystalline materials with high resolution, such as difficult-to-crystallize proteins. In general, the required incident intensity is predicted to scale inversely with the desired resolution d as d^{-4} (see [8]). In the case of protein molecules, the integrated intensity required to solve the structure with a desirable resolution exceeds the Henderson limit for radiation damage. However, unlike the case of imaging individual cells where the sample is unique, with protein a series of identical particles can be introduced into the coherent beam: the total scattered intensity can be integrated while the integrated dose of any single particle will be well below the threshold for significant radiation damage [9, 10]. Spence and collaborators have been developing this 'serial crystallography' technique, where a protein solution flows through a nozzle to generate a stream of microscopic droplets containing hydrated biological samples in vacuum [9]. An elliptically-polarized laser may be used to align the molecules in the x-ray beam by inducing a dipole in order to simplify the data analysis of otherwise randomly sampled orientations.

Dynamics of materials and interfaces

The intense coherent flux available at this beamline will allow studies of the dynamics of materials and interfaces. Recently, the dynamics of fluctuations in antiferromagnetic domains was investigated using XPCS [11]. In elemental chromium, antiferromagnetism yields spin- and charge-density waves. The charge-density waves cause satellites around the Bragg peaks. When a coherent beam is used, these satellites contain information about the local domain structure. By monitoring the fluctuation of the speckles in these peaks, the dynamics of domain wall motion can be studied as a function of temperature. This particular study found that domain wall motion is thermally activated at high temperatures, but when cooled below 40 K, the rate of domain wall motion plateaus, consistent with an activation mechanism rooted in quantum fluctuations.

The above experiment investigated correlations in time for a given scattering condition. With the high coherent flux at the ERL, each coherent scattering pattern in this time-resolved experiment could be inverted to yield detailed time-resolved structural information about the system. Wochner and colleagues recently reported that higher order cross-correlation analysis can yield hidden local symmetries [12]. For example, the authors developed an angular cross correlation function that revealed 4-, 5-, 6- and 10-fold symmetry in colloidal glass. They also reported temporal relaxation behavior with the evolution of 6-fold to 5-fold symmetry. Their approach has profound potential for studies of the nature of the glass transition.
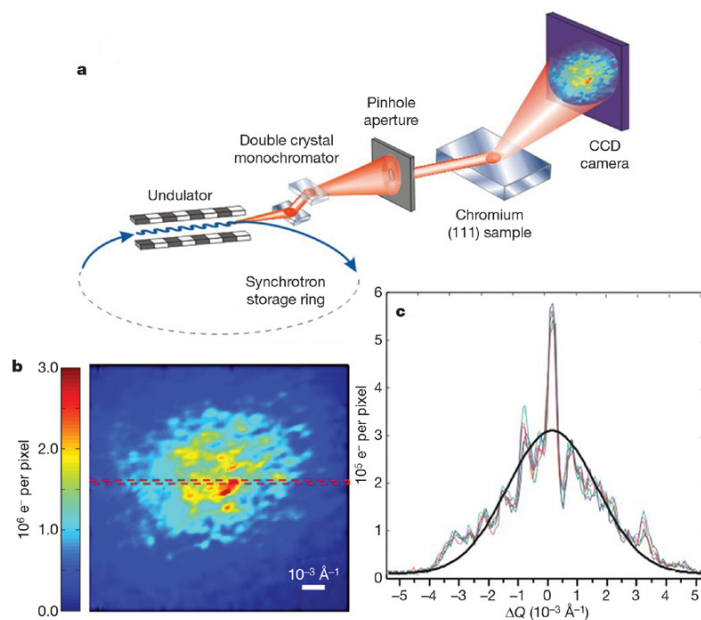

Figure 3.4.3: Coherent scattering from a charge-density-wave satellite peak yields information about the local domain structure of antiferromagnetic chromium. Image reproduced from [11]

Coherent imaging of nanocrystals

When a small crystal is coherently illuminated by x-rays, the crystal's sharp Bragg peaks are replaced by complex diffraction patterns centered about each Bragg peak which encode the shape [13] of the crystal and any deformation of its crystal lattice [14]. These patterns can be measured in three dimensions by rocking the crystal through a small angular range ($< 1°$) or scanning the photon energy through a narrow range. Iterative routines are then used to recover the phase of the complex wave field producing the diffraction, and simultaneously recovering the electron density and a strain projection inside the sample in three dimensions.

This technique holds potential for imaging crystalline samples that are surrounded by a matrix of an alternate material or even surrounded by the same crystalline material with an alternate orientation which diffracts in a different direction. A single Bragg peak will still contain information only about the crystallite of interest. Additionally, the strain sensitivity could be used to measure interfacial effects with very high sensitivity.

There is great interest in the high-pressure community to extend the coherent imaging technique to samples under pressure in a diamond anvil cell. This beamline will provide unprecedented coherent flux at relatively high energies. If other technical challenges can be overcome, such as how to deal with wavefront distortions introduced by the diamonds or the gasket material, it will be possible to map strain fields in samples under high pressure using coherent diffractive imaging.

Coherent tomographic imaging of extended objects

While ultimate resolution is a strength of imaging with electron probes, imaging of thicker samples will be a unique strength of x-ray probes. The ERL will be uniquely capable of imaging larger samples, due to the high coherent flux and penetrating power of hard x-rays. Recently, a new technique called ptychography has been developed to deal with the constraints of coherently imaging extended samples [15]. The sample is scanned through the coherent beam, and the overlap of neighboring illuminated regions provides the constraints to solve the phase problem as illustrated in Fig. 3.4.4. The first extension of the ptychographic technique to tomography has recently been reported, providing access to lower-contrast features inside bone that are not visible with absorption contrast alone [16]. This technique will be greatly enabled by the ERL due to orders of magnitude improvement in coherent flux at high energies.

3.4.4 X-ray Source

New third-generation synchrotron sources are now nearly fully coherent in the vertical direction and incoherent in the horizontal due to the pancake-shaped electron source. A coherent fraction of the source is selected using a pinhole, such that the vast majority of the total intensity is not used, in order to yield a partially coherent beam.

With its round, low energy-spread electron beams, the ERL is capable of taking full advantage of long undulators, generating high-intensity coherent beams. The shape of the source allows new undulator designs to be considered. For the high-brilliance beamline, we are considering a new, flexible insertion device called a Delta-type undulator. This device can provide horizontally, vertically, or helically polarized x-ray beams. Most experiments at this beamline will be brightness-limited, so the spectral brightness should be as high as possible:
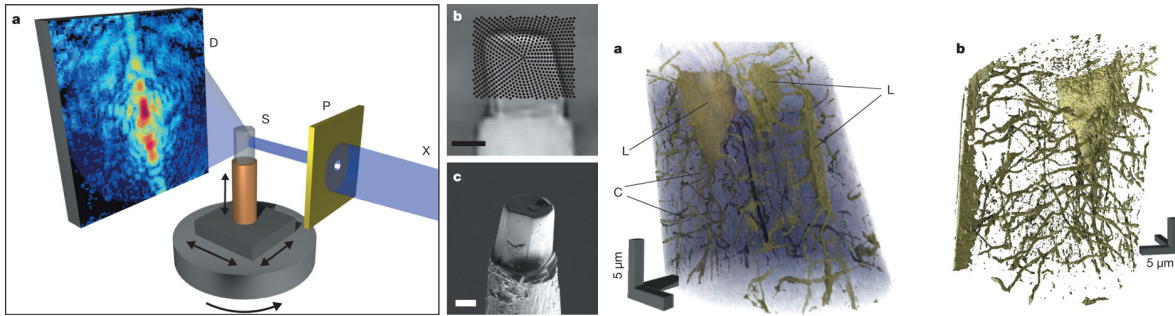
Figure 3.4.4: Ptychographic coherent imaging of a thick, extended bone sample. The technique provides volumetric information based on absorption and phase contrast, enabling studies of complex sample matrices. For details, see [16].
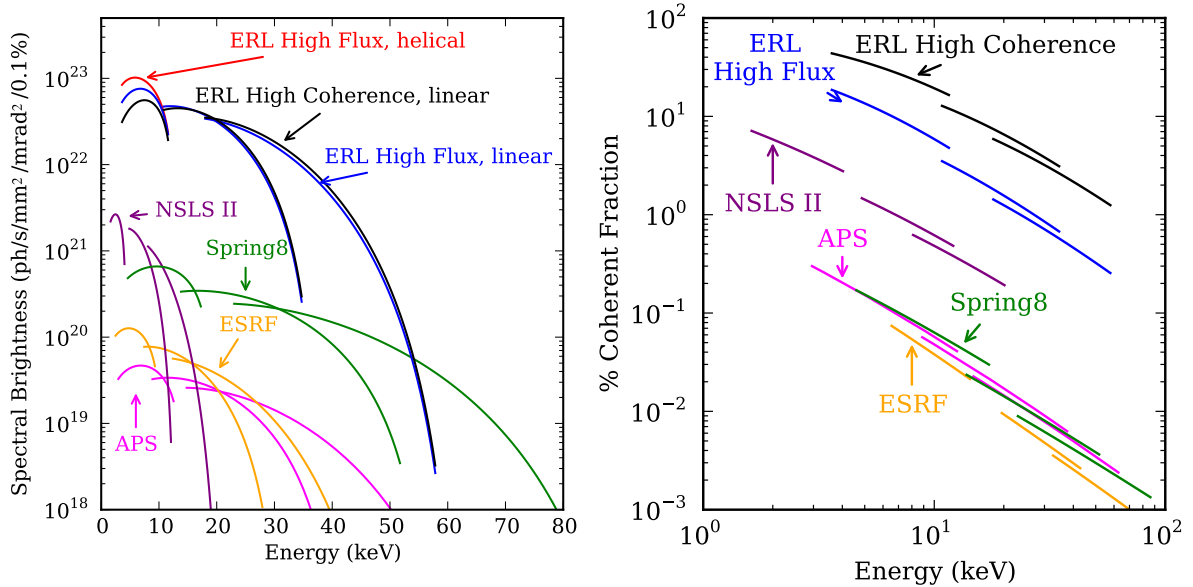

Figure 3.4.5: Nominal spectral brightness and coherent flux for various sources, as predicted by SPECTRA using the parameters listed in Table 3.4.1, are shown on the left graph. ERL modes (e.g., 'High Flux') are listed in Table 3.4.1; 'helical' and 'linear' refer to undulator modes described in §2.7.3. Comparison of nominal coherent fraction (%) for various sources is displayed on the right graph.

1×10^{23} photons/s/mm^2/mRad^2/0.1% bandpass appears to be achievable at $8\,\mathrm{keV}$. The insertion device should provide continuous coverage of energies over $\sim 4\,\mathrm{keV}$. Integrated *coherent* flux at $8\,\mathrm{keV}$ is projected to be on the order of 5×10^{14} photons/s.

The undulator is expected to be approximately 25 meters long, with a 5 mm bore and 19 mm period. This short-period device will generate high-intensity x-ray beams of $4\,\mathrm{keV}$ and greater, and provide harmonic overlap for high-energy applications.

This beamline is being designed to take full advantage of all three modes of operation at the ERL: high coherence, high flux, and short pulse. High-coherence and high-flux experiments will benefit from a quasi-continuous source: the $1.3\,\mathrm{GHz}$ repetition rate is required. β should be tunable between 4 and 25 meters, in order to maximize brilliance or decrease the (already low) divergence. This beamline is not located in a portion of the facility that is capable of generating $50\,\mathrm{fs}$ x-ray pulses, but the natural $2\,\mathrm{ps}$ pulse length still provides scientific opportunities during short-pulse operation.

Because of the short-pulse length ($2\,\mathrm{ps}$ RMS) and high-repetition rate ($1.3\,\mathrm{GHz}$), the ERL time structure will be closer to that of a continuous source than existing storage rings. This is very helpful for XPCS experiments with time resolution below 1 μs. One reason is that intensity-intensity correlations, the 2nd order degree of coherence, denoted $g^{(2)}(\tau) = \langle I(t) \cdot I(t + \tau) \rangle / \langle I(t) \rangle^2$, contains much information on temporal correlations in the scattering system, however, the measured $g^{(2)}(\tau)$ is a convolution that includes fluctuations in both the sample and 'apparatus', including the source. A short-exposure interval samples high-frequency noise on the incident beam, so the most favorable situation occurs when even the shortest exposure averages many x-ray pulses, each of which may have been generated by electron bunches with (hopefully random) charge fluctuations. In practical terms a 1 μs exposure averages 1300 ERL pulses, while at the APS in 24-bunch (top-off) mode only 6.4 bunches contribute, and in the most favorable mode, 1296-bunch (no top-off), approximately 350 bunches are averaged.

Third-generation sources typically keep some fraction of the electron buckets empty to mitigate ion trapping. Such features in the source time structure present a fundamental challenge for studies of fast dynamics. As seen in Fig. 3.4.6, when the timescale of interest τ approaches that of the time structure of the source, the source itself contributes significantly to the value of interest $g^{(2)}$.

This problem could possibly be overcome by synchronizing data acquisition with the source time structure at existing facilities or measuring correlations in the incident beam, adding complexity to an already difficult experiment. The plan for the ERL is to use ion-clearing electrodes to mitigate ion trapping. As a result, the ERL source will be truly quasi-continuous below the 10 ns timescale, which will be important to fill the capability gap between existing XPCS and inelastic scattering techniques.

We do not yet know the degree of bunch-to-bunch charge fluctuations at the ERL. A likely source of noise will be the stability of the lasers used to generate the electrons from the photocathode. A preliminary goal is to limit bunch-to-bunch charge fluctuations to $< 1\%$.
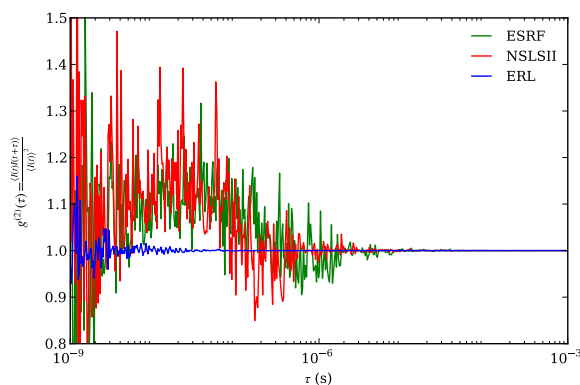
Figure 3.4.6: Simulated intensity correlations as a function of delay time τ for different sources. For studies of dynamics at time scales less than 1 μs, the time structure of existing sources (used to mitigate ion trapping) becomes a significant contribution to noise. The ERL is expected to be quasi-continuous down to the 10 ns level.

3.4.5 Conceptual design of coherent diffraction beamline

Beamline layout

The proposed 25 m insertion device would generate an extremely narrow beam with high power density, so an aperture or set of slits such as proposed for the Coherent Hard X ray (CHX) beamline at NSLS-II will be used to pass the central cone but filter the off-axis power to protect downstream optical elements. When the undulator operates in helical mode, the higher-order harmonic intensity occurs off-axis.
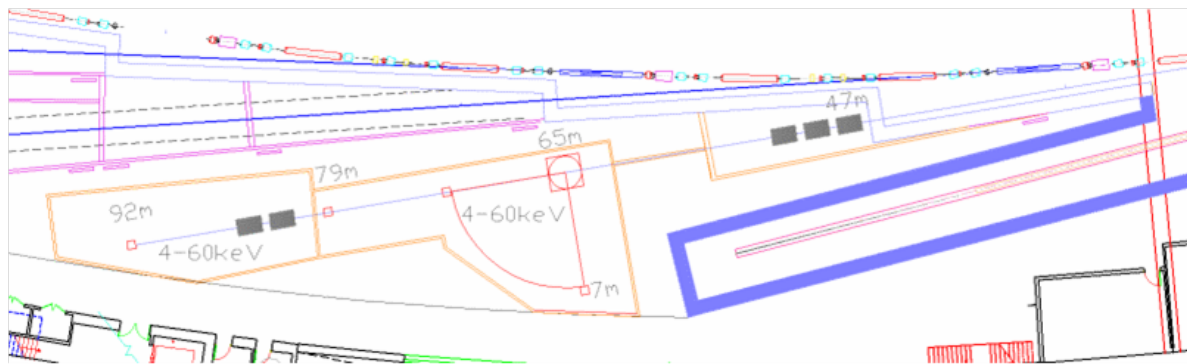

Figure 3.4.7: Floor plan for coherent diffraction beamline including an optics enclosure and two experimental hutches, both designed to allow use of the undulator's fundamental and higher harmonics. The first experimental hutch includes a diffractometer with a 7 m long detector arm that can be positioned in the horizontal plane. The detector arm in the forward-scattering direction will be 15 m. Experiments can be prepared in the second hutch while the first hutch is in use.

If possible, it is highly desirable to preserve the optical axis of the x-ray beam to allow both

of the experimental stations shown in Fig. 3.4.7 to use either monochromatic or 'white' beam. The potentially optics-less configuration would take advantage of the full on-axis flux of the first harmonic of the undulator in helical mode, while higher harmonics are suppressed. The first experimental hutch, Fig. 3.4.7, will include equipment designed for XPCS and CDI in both with forward and Bragg geometry. The second experimental hutch, see §3.4.6, will be accessible while the first hutch is in use, making it suitable for non-standard experiments or those which require *in-situ* sample preparation.

The optics enclosure, located immediately after the ratchet wall, will provide a dispersive four-bounce monochromator that directs monochromatic beam along the original pink-beam optical axis. The monochromator can be removed for pink-beam operation in order to take advantage of the full harmonic bandwidth of the undulator, which at 0.2% is already sufficiently monochromatic for many experiments and provides a significant improvement in flux.
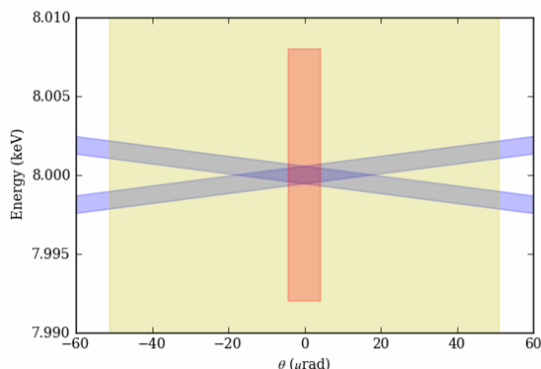
Optical design

Figure 3.4.8: A DuMond diagram illustrating the distribution and bandpass of intensity. The natural opening angle for the ERL operating at 5 GeV is illustrated by the beige patch. Constructive interference in the undulator yields a harmonic at 8 keV with intensity distributed in energy and angle in the red area. The intensity passed by a non-dispersive double-bounce Si-111 monochromator is represented by the intersection of one of the blue areas with the red area. The intensity passed by a dispersive four-bounce monochromator is represented by the intersection of the darker blue diamond with the red area.

The optical design should be flexible enough to allow high-energy operations. The beamline is projected to provide as much coherent flux at 40 keV as the NSLS-II CHX beamline will provide at 10 keV. X-ray mirrors should therefore be optional components. It should be possible to operate the beamline in an 'optics-less' mode. Ideally, the optics should preserve the original optical axis of the undulator, allowing switching between modes without major realignment, allowing for the design of more stable downstream components.

One approach to provide such flexibility is to employ a dispersive 4-bounce monochromator to preserve the original optical axis. The natural divergence of the x-ray beam is nicely matched with the bandpass of a dispersive 4-bounce Si-111 monochromator, as seen in Fig. 3.4.8,

such that there is practically no intensity loss when compared with non-dispersive 4-bounce monochromator, although the theoretical reflectivity of Si-111 is around 80% at 5 keV and over 90% at 10 keV, so two additional bounces will diminish the total intensity to some degree.
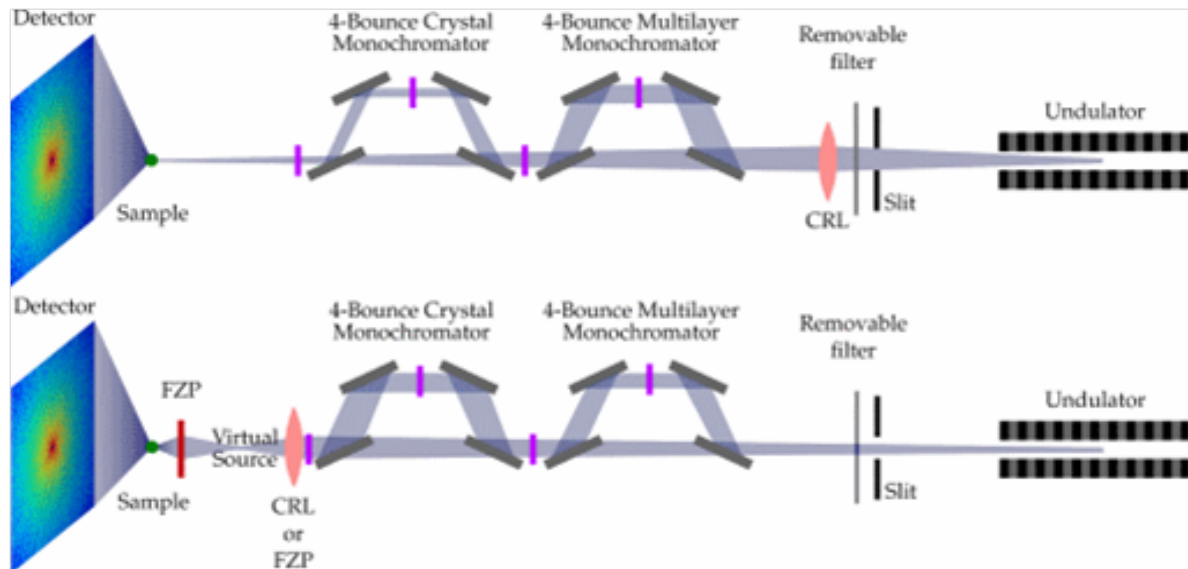

Figure 3.4.9: Four-bounce monochromator (crystal or multilayer) for improving the undulator energy resolution. Compound refractive lenses or Fresnel zone plates can be inserted for focusing.

If current efforts in the community to develop wavefront-preserving multilayer optics are successful, one could imagine adding a multilayer monochromator stage to the optics design in order to provide an intermediate level of monochromaticity between crystals and pink-beam. Since multilayers operate at lower angles, the incident power density on the first multilayer would be more manageable than with a crystal optic, especially at lower energies. Compound refractive lenses are envisioned for the CHX beamline at NSLS-II and a similar scheme is equally applicable here. A compound refractive lens could be placed upstream of the monochromator to provide 2:1 demagnification at the sample position (and also to serve as a high-pass filter to mediate the heat load on the first monochromating optic.) Alternatively, a focusing optic with higher divergence could be placed further downstream to provide a virtual source that could be reimaged to provide greater control over the beam size at the sample position. Such flexibility would provide the ability to adjust the beam size over the range of 100 nm to 10 μm. An optical layout that would provide the desired flexibility is illustrated in Fig. 3.4.9.

The monochromators will need to be extremely stable. For XPCS experiments with time resolution approaching 10 ns, the monochromator should be so stable that it does not cause the beam to appreciably shift its position at the sample. At third-generation sources, a pin-hole is used to select a coherent fraction of the beam: thus the experiment is less sensitive to monochromator instabilities as long as the pinhole is stable and uniformly illuminated. At the ERL, where the beam may be as high as 20-30% coherent at 10 keV, one would like to use the full beam for XPCS and therefore stability will be critically important. Side-bounce monochro-

mators may prove to be more stable than the vertical monochromators commonly found at third-generation sources. Side-bounce monochromators are also desirable since the undulator can operate in a vertical polarization mode, thus large diffractometers can be considered that scatter into the horizontal, rather than vertical, plane.

3.4.6 Hutch/instrument design

Hutch 1: Small angle coherent scattering, imaging and dynamics

The first hutch is designed to focus on coherent small-angle scattering techniques including coherent imaging and x-ray photon correlation spectroscopy. A cleanup aperture appropriate for the virtual source will be installed at the upstream end of the hutch, followed by a stage bearing various condensing zone-plate optics optimized to cover the $4 - 15$ keV energy range and an order-sorting aperture. The zone plate and sample stages will be adjustable along the optical axis in order to scan the focus through the sample, allowing for Fraunhofer and Fresnel coherent diffraction imaging techniques. This beamline is envisioned to be vacuum compatible to meet the needs of serial crystallography, coherent imaging of frozen hydrated biological samples, but also compatible with alternative sample environments or ambient conditions by interchangeable sample chambers and stages. In order to accommodate Fresnel diffraction imaging, care must be taken such that the beam and sample positions are stable in order to yield the highest possible resolution and avoid introduction of artifacts.
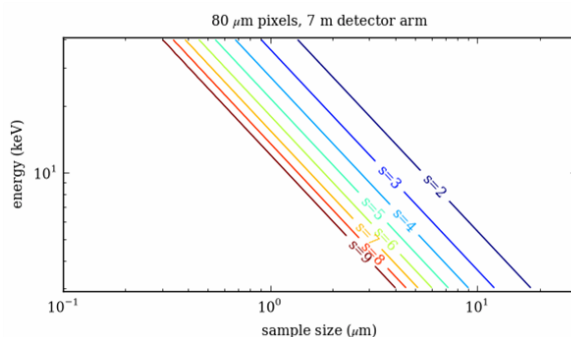

Figure 3.4.10: Relationship between incident energy and maximum sample size for which a far field diffraction pattern can be sampled with a sampling ratio s using a detector with 80 μm pixels located 7 m from the sample. A minimum sampling ratio of 2 is required for unique sample determination.

There are two main considerations in determining the optics-sample stability required by a Fresnel CDI experiment. The first is a shifting of the diffraction pattern in the plane of the detector which is equal to the shift of the sample times of the magnification factor produced by the diverging wavefront. While this effect is present in all coherent diffraction, the consequence in plane wave CDI is that the sample must not move by a significant fraction of a detector pixel, which is typically on the order of 10 microns. In Fresnel CDI, the magnification, given by the ratio of the sample-detector distance to the focus-sample distance, can be on the order of a thousand. This leads to a stability requirement on the order of ten nanometers.

A more complicated consideration is due to additional structure in the illuminating wavefield beyond the spherical phase curvature, which gives rise to the magnification. Any changes in the wavefield with a magnitude (of amplitude or phase) comparable to the sample contrast will create artifacts. This leads to the requirement that the sample and optic must be stable to better than the length scale of any non-uniformities in the illuminating wavefield over the acquisition time. Detailed knowledge of the relative motion over the time of a single exposure may in principle be used to deconvolve the motion from the sample transmission function.

We intend to build upon the progress made at APS 34-ID-C. This hutch will include a four-circle diffractometer that can accommodate an ultra-high vacuum system permitting in-situ sample growth and characterization. An alternative (non-vacuum) configuration could allow observation of the sample with a confocal optical microscope, allowing the sample to rotate through large angles while keeping the region of interest centered in the x-ray beam. The undulator can produce vertically polarized x-rays, which allows some simplification of the diffractometer design while improving stability. The diffractometer will be equipped with a 7-m long detector arm sweeping in the horizontal plane for performing coherent diffraction from crystalline samples.

The length of the detector arm is an important consideration since it impacts the design for the hutch. The length of the detector arm L can be determined for a diffracting sample with maximum cross-section length a, measured by a detector with a pixel size p located L away from the sample, and oversampling ratio s:

$$L = \frac{asp}{\lambda} \tag{3.4.1}$$

Assuming a desired sample diameter of $10\,\mu$m and a detector pixel size of $80\,\mu$m, the minimum detector distance to oversample ($s = 2$) a diffraction pattern ranges from $5.3\,$m (at $4\,$keV) to $19\,$m (at $15\,$keV). As seen in 3.4.10, with a $7\,$m detector distance, the constraints for minimum oversampling limit maximum sample size to $25\,\mu$m at $4\,$keV and $4\,\mu$m at $15\,$keV. If detectors with $40\,\mu$m pixels are developed, a $4\,\mu$m particle could be imaged at $30\,$keV with minimum oversampling.

The pixel size of the reconstructed images of the sample transmission function will be equal to twice the maximum sample size divided by the number of pixels. The design of the diffractometer must therefore permit flexibility in the detector distance. It is necessary to position and hold the detector stable to a small fraction of the pixel size, and while this is not a challenging task for $80\,\mu$m pixels, future detectors may have significantly smaller pixels. For a large detector arm, which must support a vacuum flight path between the sample and detector, we envision a design similar to what is seen with neutron diffractometers where the detector arm sweeps out an arc in the horizontal plane. The detector will be positioned at an appropriate location along the length of the detector arm, with a vacuum flightpath conveying to the sample.

The sample should have three axes of rotations to permit crystallographic orientation as well as sub-micron precision positioning in x, y, and z. Ideally, the sample would have fine translations above the axes of rotation to position the sample region of interest in the beam as well as motions below the rotation axes to align the diffractometer with the beam.

Hutch 2: Flexible experimental endstation

The second hutch would be accessible while experiments are conducted in the first hutch, allowing time to set up many different kinds of experiments and thus explore new techniques. A Laue monochromator inspired by the design used at the ESRF ID15 High-Energy Scattering Beamline could be installed at the upstream end of the hutch to provide a narrow bandpass, which would limit the lower end spectrum to energies above $\sim 15\,\text{keV}$, depending on the thickness of the crystals, but would allow more advanced scattering geometries for surface scattering. The crystals would provide sagittal focusing in one direction, and a beryllium compound refractive lens could provide focusing in the orthogonal direction.

At high energies, it may be possible to explore coherent scattering from samples in extreme environments, such as at high pressure in diamond anvil cells. Dynamical processes of surfaces and interfaces could also be studied with brilliant, low-divergence, high energy beams.

This hutch could support experiments in the short-pulse mode of operation, although given the location of this beamline, bunch compression will not be possible and therefore experiments will make use of the inherent 2 ps pulse length. One experiment that could benefit from this time structure is x-ray scattering studies of protein structural dynamics in solution, which were recently reported with 100 ps time resolution [17].

3.4.7 Detectors

Advanced area detectors, such as those under development at Cornell, the Paul Scherrer Institut, and CERN, will be required in order to take full advantage of the opportunities in coherent diffraction at an ERL source. The specific detector requirements will depend on the application. Quantitative measurement of weaker scattering intensity at high angles, which contains the high-resolution information about the sample, requires a detector with single-photon sensitivity. The intensity in a coherent diffraction pattern can span many orders of magnitude, therefore a large dynamic range and limited dead time affect the efficiency of a CDI experiment and the speed of an XPCS or dynamic CDI experiment.

For serial crystallography, imaging of frozen hydrated samples, and experiments requiring lower energy x-rays, we envision using pixel array detectors that mate to the vacuum system following an interchangeable vacuum flight path. For XPCS experiments, a pixel array detector with on-chip time autocorrelators is desirable. High-energy scattering experiments would make use of CCD's using phosphors designed for good quantum efficiency with high-energy x-rays.

References

[1] Weitkamp, T., *et al. X-ray wavefront analysis and optics characterization with a grating interferometer.* Applied Physics Letters, **86** (5), 054101 (2005). doi:10.1063/1.1857066.

[2] Handa, S., *et al. Novel Scheme of Figure-Error Correction for X-ray Nanofocusing Mirror.* Japanese Journal of Applied Physics, **48** (9) (2009).

[3] Mimura, H., *et al. Breaking the 10 nm barrier in hard-X-ray focusing.* Nature Physics, **6** (2), pages 122–125 (2010).

[4] Shapiro, D., *et al. Biological imaging by soft X-ray diffraction microscopy.* Proceedings of the National Academy of Sciences of the United States of America, **102** (43), pages 15343–6 (2005).

[5] Chapman, H. N., *et al. Femtosecond X-ray protein nanocrystallography.* Nature, **470** (7332), pages 73–77 (2011).

[6] Huang, X. J., *et al. Soft X-Ray Diffraction Microscopy of a Frozen Hydrated Yeast Cell.* Phys. Rev. Lett., **103** (19) (2009).

[7] Howells, M. R., *et al. An assessment of the resolution limitation due to radiation-damage in X-ray diffraction microscopy.* Journal of Electron Spectroscopy and Related Phenomena, **170** (1-3), pages 4–12 (2009).

[8] Shen, Q., I. Bazarov, and P. Thibault. *Diffraction imaging of nonperiodic materials with future coherent x-ray sources.* J. Synchrotron Rad., **11** (19), pages 438–438 (2004).

[9] Spence, J. C. H. and R. B. Doak. *Single Molecule Diffraction.* Phys. Rev. Lett., **92** (19), page 198102 (May 2004). doi:10.1103/PhysRevLett.92.198102.

[10] Starodub, D., *et al. Dose, exposure time and resolution in serial X-ray crystallography.* Journal of Synchrotron Radiation, **15**, pages 62–73 (2008).

[11] Shpyrko, O. G., *et al. Direct measurement of antiferromagnetic domain fluctuations.* Nature, **447** (7140), pages 68–71 (2007).

[12] Wochner, P., *et al. X-ray cross correlation analysis uncovers hidden local symmetries in disordered matter.* Proceedings of the National Academy of Sciences of the United States of America, **106** (28), pages 11511–11514 (2009).

[13] Williams, G. J., *et al. Internal structure in small Au crystals resolved by three-dimensional inversion of coherent x-ray diffraction.* Phys. Rev. B, **73** (9) (2006).

[14] Pfeifer, M. A., *et al. Three-dimensional mapping of a deformation field inside a nanocrystal.* Nature, **442** (7098), pages 63–66 (2006).

[15] J. M. Rodenburg and H. M. L. Faulkner. *A phase retrieval algorithm for shifting illumination.* Appl. Phys. Lett., pages 4795–4797 (2004). Vol. 85 (20).

[16] Dierolf, M., *et al. Ptychographic X-ray computed tomography at the nanoscale.* Nature, **467** (7314), pages 436–439 (2010).

[17] Cho, H. S., *et al. Protein structural dynamics in solution unveiled via 100-ps time-resolved x-ray scattering.* Proceedings of the National Academy of Sciences of the United States of America, **107** (16), pages 7281–7286 (2010).

3.5 Nanobeam small- and wide-angle scattering beamline

3.5.1 Microbeam scattering beamline

In scattering experiments with x-ray microbeams, two seemingly contradictory requirements need to be reconciled: obtaining the smallest possible spot size for optimum real-space resolution and obtaining the lowest possible divergence for high reciprocal space resolution. This makes an ultra-low emittance x-ray source such as an ERL the ideal place for such experiments. The emittance, the product of beam size and divergence, is the phase space invariant of the x-ray optical system. Hence beam size can be traded with divergence and vice versa, however, both cannot be minimized simultaneously without serious loss of x-ray flux [1]. Hence only a beamline with exceptional spectral brightness can achieve significant progress in such applications.

The ERL source properties would also allow obtaining unprecedented coherent beams of a few nm size [2] which will enable novel scanning applications (fluorescence tomography, Coherent X-ray Diffraction Imaging) on hierarchically organized materials. Such materials are not accessible to the current generation of third-generation SR sources.

A microbeam scattering beamline for soft materials will be designed and optimized for SAXS and USAXS with x-ray microbeams as well as WAXS and GISAXS using nanobeams. With endstations optimized for soft matter, the beamline would bring current microbeam applications at third-generation SR sources [3] to their full fruition and bridge the gap between focal spot size and maximum scattering resolution at an excellent x-ray flux. Moreover, an ERL source would enable new science, such as covering the full range of length scales in hierarchical materials, probing fast structural kinetics of extremely weak scatterers, such as proteins in a microfluidic environment [4, 5] and liquid crystals [6] in the early stages of ordering, as well as facilitating fast time-dependent studies, which are out of reach at current conventional sources.

3.5.2 Applications

Complex structures in biology and medicine as well as in materials science, environmental science, or food science are essentially heterogeneous. For such systems the optimum beam size is determined by several times the repeat distance of the structure to be studied. Hence for block copolymers with domain sizes of 30 nm to 300 nm, microbeams of about $1 - 5\,\mu m$ diameter are desirable. For ordering in nanostructured materials with a liquid crystalline component, the Bragg d-spacings are commonly between 1 to 5 nm, so nanobeams of 10 to 50 nm would be of high interest. With an ERL source these theoretical limits could be reached while maintaining a high flux from the source.

One of the high-profile applications of x-ray micro- and nanobeams is probing complex materials in biology and materials science with microbeam SAXS/WAXS. Real-space scanning of the sample and SAXS/WAXS from a small sample volume are combined to study heterogeneous structures such as wood, bone, and muscle from the molecular scale (scattering) to the macroscopic scale (scanning).[7, 8] An example for a scanning SAXS/WAXS experiment for a hierarchically organized high-performance fiber Kevlar is shown in Fig. 3.5.1 [9]. The fiber section was scanned on-axis with a $1\,\mu m$ beam in transmission geometry. Skin-core structures are observed both for the WAXS and the SAXS composite images. Such images provide detailed information on local disorder and processing conditions.
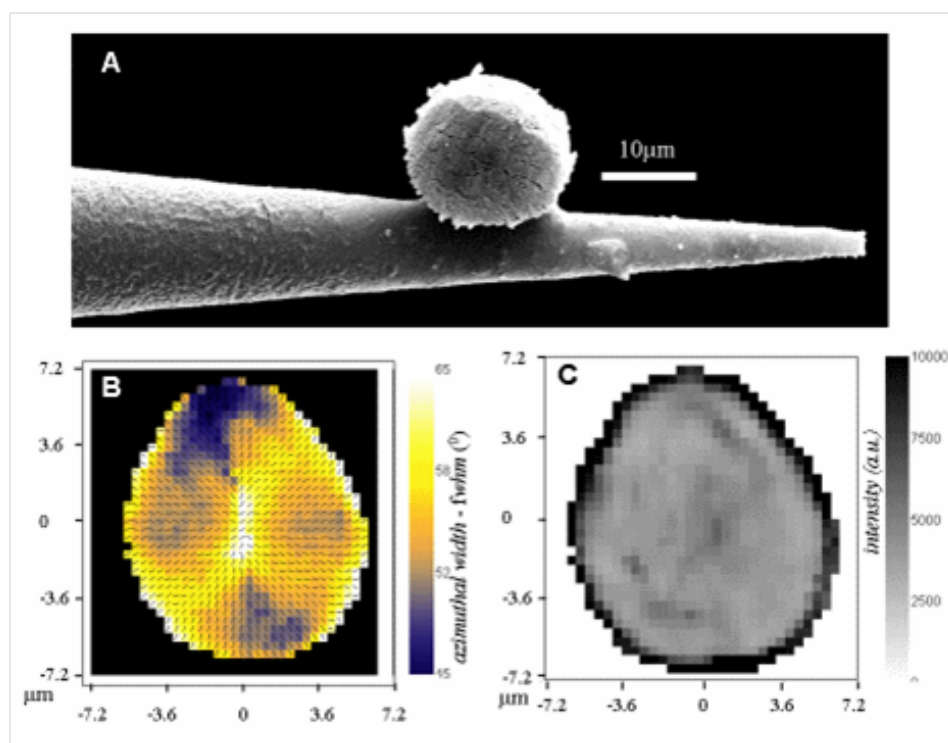
Figure 3.5.1: A: on-axis scanning electron microscopy image of laser-cut Kevlar-29 section glued to glass capillary, B: composite WAXS image of azimuthal width and radial texture based on a recursive analysis of the 200 reflection. The individual patterns were recorded with a $1\,\mu$m beam. The skin zone shows more disorder; C: composite SAXS image of intensity of central scattering. The increased intensity in the skin-zone can be attributed to an oriented SAXS streak. An ERL soft matter beamline would allow studying skin-core structures on smaller fiber cross sections such as in electrospun fibers.

Other emerging high-profile applications include micro- and nano-fluidics for studying fast structural kinetics in solution [4–6] as well as grazing-incidence wide-angle and small-angle x-ray scattering (GIWAXS/GISAXS) studies of thin films with concentration gradients [10–12]. Thin film structural studies will be of particular interest in the emerging area device structures in organic electronics [13]. Thin-films are the preferred approach to build devices such as biosensors, solar cells, or solid-state lighting.

Recently, grazing-incidence scattering has revealed a wealth of information on nanostructured thin films [14–17] and films of semiconducting molecules and polymers in the field of organic electronics [18–21]. For such real devices, probing locally small areas under grazing incidence (scanning GISAXS, scanning GIWAXS) would be extremely illuminating. Patterning of devices [14, 22, 23] and integration of organic components into micro-scale circuits poses new challenges to structural analysis, for which microbeams are ideally suited. First successful demonstrations have been reported [24], however, there still remains a plethora of phenomena to be investigated. Furthermore microbeams in grazing incidence could be utilized to study
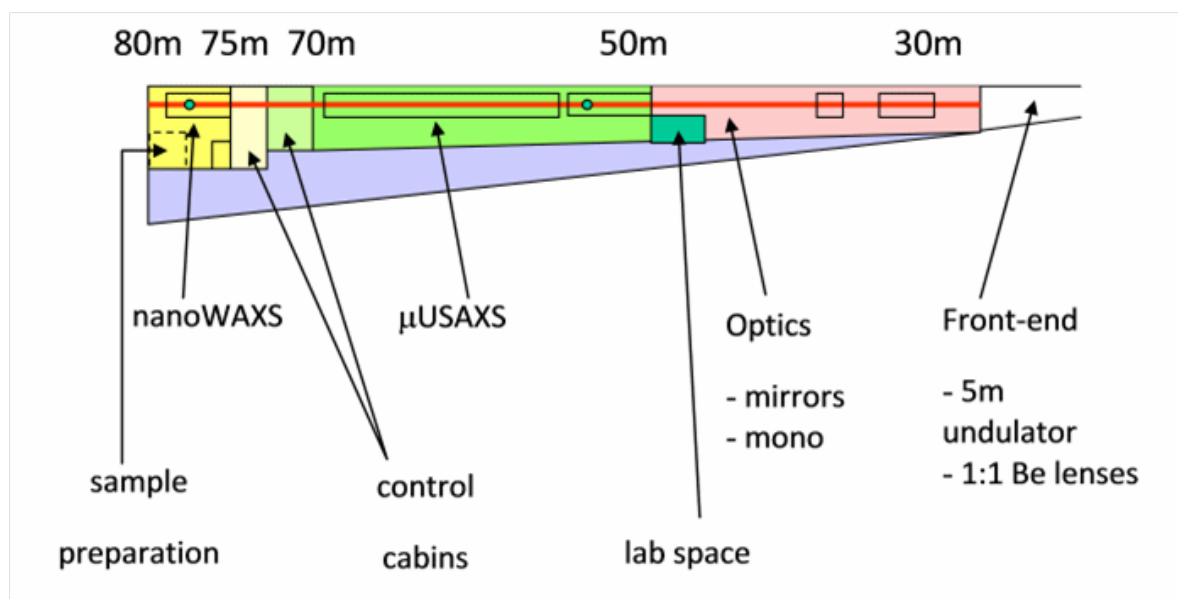
Figure 3.5.2: Possible layout for a microbeam scattering beamline.

curved surfaces locally. This may be particularly interesting for biological applications, as surfaces such as cell walls or intracellular vesicles are not flat but often have a curvature in only one direction. Again, biological systems offer many challenging problems that x-ray micro and nanobeam may be able to tackle.

3.5.3 Beamline layout

The layout of a microbeam scattering sector is dictated by balancing spot size against angular resolution. For mesoscopic structures such as block copolymers, spot sizes of $100\,\text{nm}$ to $10\,\mu\text{m}$ are needed to detect local structures with periods on the order of $10\,\text{nm}$ to $1000\,\text{nm}$. Thus sample-to-detector distances from $1\,\text{m}$ to $15\,\text{m}$ are needed, while the source-to-sample distance can be at $50\,\text{m}$ (small-angle scattering and ultra small-angle scattering). In contrast, for the smallest beamsizes of $10 - 100\,\text{nm}$ the maximum source to sample distance of $75\,\text{m}$ is required, while a resolution of $1\,\text{nm}$ to $10\,\text{nm}$ is sufficient (wide-angle scattering). Both of these regimes can be achieved with a two hutch design as shown in Fig. 3.5.2. A hybrid application will be scanning GISAXS to characterize the local structure in thin films and organic electronics devices. Scanning GISAXS requires a very small beam height vertically, while the horizontal focusing is given by the required lateral resolution. Both requirements can be met in the downstream nanobeam hutch provided that a $1\,\text{m}$ to $1.5\,\text{m}$ sample-to-detector distance is supported. This split of the science program into two hutches is further motivated by the very different line-up, set-up, and stability requirements. For spot sizes of $1\,\mu\text{m}$ and up for microUSAXS, optical microscopy can still be employed to aim the x-ray beam, while elaborate conditioning of the beam upstream is mandatory to achieve the required resolution. Part of this aperture and focusing system can be accommodated in the upstream optics hutch. For nanoWAXS, x-ray detectors and auxiliary equipment need to be placed

close to the sample. Hence the microSAXS and the nanoWAXS set-ups have necessarily quite a different configuration. Moreover, sample manipulation, temperature stabilization and vibration insulation are much more stringent for nanoWAXS. [25, 26]. Hence the latter instrument requires dedicated equipment in a separate hutch. A tentative lay-out based on these considerations is shown in Fig. 3.5.2.

The frontend and beamline are to be kept windowless. Windows, even if polished, are known to distort x-ray wavefronts and cause loss of coherence and homogeneity of the beam. Moreover, the power density of the ERL beam would cause significant challenges for window cooling, which may make high performance materials such as thin, single-crystalline Be or diamond windows mandatory.

3.5.4 Source and frontend

The low-energy spread of the ERL electron beam has the effect that ERL undulators will radiate coherently over lengths of 5 m and more. Thus a 5 m undulator with a 20 mm period will have a bandwidth of only 0.4% on the first harmonic. Thus 'optics-free' schemes can be devised, which make the use of monochromators as well as mirrors unnecessary for a large class of experiments (all types of SAXS and WAXS save anomalous scattering). Such schemes not only would preserve the source coherence in a natural way; they would also reduce the cost of the beamlines as the amount of costly coherence-preserving optics may be reduced in many cases.

The source for the Microbeam Scattering Beamline will be a 5 m undulator. Several types of undulators have been anticipated:

1. The ultimate source for 'optics-free' operation would be a helical undulator. A helical undulator radiates only on the first harmonic on axis. Hence for such a source the energy spectrum could be continuously tuned. Moreover, in such a device, the polarization can be tuned from circular to linear. A design effort for such a source is under way as described in §2.7.3.

2. An initial device for 'optics-free' operation would be a 5 m planar in-vacuum undulator with a 20 mm period. This undulator would radiate at a fixed photon energy of 10 keV in a low-K mode (K< 0.3) that essentially produces only radiation on the first harmonic with a bandwidth of 0.4%. Such a device would be ideally suited for SAXS and WAXS type experiments. Hence the flux loss while operating in low-K mode will be more than compensated by the fact that only 'useful' photons will be generated that do not need primary optics such as mirrors and monochromators. The microbeam scattering station will be a test bed to explore this 'optic-free' mode.

3. A planar or helical in-vacuum undulator combined with primary optics. In order to achieve the smallest beam sizes at the focal spot, the x-ray beam needs to be monochromatized for use with dispersive focusing optics such as Fresnel zone plates, multilayer Laue lenses or compound reflective lenses. In this case, the undulator can be tuned, and a planar undulator could be operated at various harmonics ($1^{st}, 3^{rd}, 5^{th}$) achieving high flux between 1 keV and 50 keV.

3.5.5 Microbeam optics

The small and round source will produce focused beams with identical size and divergence in both the horizontal and vertical scattering plane. The ERL source size of only $5\,\mu m$ will be the perfect source for micro- and nanobeam generation, while the initial low divergence of the photon beam will provide good scattering resolution even after focusing. Moreover, the low divergence of the photon beam will limit the growth of the beam cross section, so that even at a long distance from the source, the beam size will still be well matched to the small incident aperture of focusing devices such as KB mirrors, compounds refractive lenses, and Fresnel zone plates, and will thus produce ample flux in the focal spot. This eliminates the necessity for a secondary source that would cost resolution.

3.5.6 Hutch requirements

Microbeam hutch

The microbeam hutch will be the workhorse station in which microbeam experiments $(0.1 - 10\,\mu m)$ can be set-up in both a flexible and streamlined way. Optical and confocal microscopy can be used for sample positioning and line-up of microbeams. A very high x-ray flux will be provided for experiments with weak scatterers, in particular microfluidics [4, 5, 27] and droplet generators [28, 29]. The high flux will also be instrumental for experiments demanding short time resolution down to microseconds. A special development project will be USAXS with microbeams.

The elongated 20 m microbeam hutch provides extended space to house a 15 m flightpath for ultrasmall-angle scattering (USAXS) with microbeams and space for one or two SAXS area detectors (high dynamic range and low noise, fast detection) and a WAXS detector close to the sample. On the upstream side a 5 m optical table houses flexible space for microbeam optics and a six-axis sample stage with grazing-incidence scattering capability $(x, y, z, \theta, \chi, \phi)$.

Nanobeam hutch

The nanobeam hutch at the downstream end of the beamline is meant as a development station for state-of-the-art nanofocusing optics and extreme scanning and scattering applications. We anticipate that a temperature stability of $\pm 0.05\,°C$ over 8 h will be required. The goniometer should provide x/y/z scanning and rotational movements. Both large scale movements ($\leq 50\,mm$ stroke; $100\,nm$ resolution) and precision movements ($\leq 1\,mm$ stroke; $1\,nm$ resolution) should be available. An integrated sample rotation (360°) and sample inclination ($\leq 5\,mrad$) will be available for diverse applications from tomography to GISAXS. The integration of optical microscopy, AFM, fluorescence spectroscopy and other spectroscopy tools (e.g. Raman) is anticipated. The detector should have the dynamic range for far field coherent x-ray diffraction imaging applications.

3.5.7 Detector requirements

Microbeam scattering area detectors should feature a high-dynamic range combined with low noise and a high frame rate. If these cannot be combined in a single instrument, two detectors

could be combined in the large SAXS tank of the microSAXS hutch, and detectors can be switched according to the demands of the experiment.

The area detector for the nanobeam hutch would primarily feature low noise and high dynamic range. Pixel size should be down to $20\,\mu$m. The sample-to-detector range should be from WAXS (about $150\,$mm) to low-resolution SAXS (about $1500\,$mm). A vacuum enclosure for sample and detector will be necessary to cut back on air scatter.

3.5.8 Optics-free beamlines

Preserving the exquisite brilliance and coherence of ERL x-ray beams poses major challenges to x-ray optics development, in particular for wavefront-preserving mirrors, monochromators, lenses and windows. For a variety of applications, however, the beam generated by an ERL undulator already has the required properties and does not require additional optics.

1. The useful length of an ideal undulator is ultimately limited by the energy spread of the electron beam. Specifically, $\delta E/E$ of the electron beam sets the minimum bandwidth of the harmonics. For the ERL, $\delta E/E \sim 10^{-4}$. Therefore, a 20 mm period undulator will radiate coherently over a length of 5m, generating x-ray beams with 0.4% bandwidth of the first harmonic. CHESS has rich experience using multilayer monochromators to create x-ray beams with bandwidths ranging from 0.3% to 2%. Many non-resonant scattering experiments are ideally matched to this range.

2. Harmonic-rejection mirrors would not be needed for either low-K planar undulators or helical undulators. Planar undulators with $K < 0.3$ emit 99% of their radiation in the forward cone into the first harmonic. The higher harmonics of a helical undulator are completely suppressed on axis.

3. Windowless, differentially pumped front-ends will eliminate wave-front distortion at windows and filters. Differentially pumped vacuum-technology for beamlines is well-developed in the soft x-ray range. With a series of differential pumping stages close to the sample, x-ray beams can be brought into an ambient environment or can be directly connected to sample vacuum systems.

4. ERL x-ray beams have such small source size and divergence that the x-ray beam spreads to no larger than 0.5 mm at 50 m from the source. Optics-free operation effectively eliminates wavefront degradation. Those experiments requiring still smaller spot sizes may, of course, focus the coherent x-ray beam with high efficiency to a very small spot size in the experimental station.

Optics-free operation leads to a paradigm shift in x-ray beamline design, where the effort would now be spent on perfecting the source (electron beam, undulator) rather than trying to further improve conventional x-ray optics, where roughness and slope error are already close to achievable fabrication limits and have become major cost factors.

References

[1] Smilgies, D.-M. *Compact matrix formalism for phase space analysis of complex optical systems.* Appl. Opt., **47** (22), pages E106–E115 (Aug 2008). doi:10.1364/AO.47.00E106.

[2] Schroer, C. G. and B. Lengeler. *Focusing Hard X-rays to Nanometer Dimensions by Adiabatically Focusing Lenses.* PRL, pages 1–4 (2005). Vol. 94 (054802).

[3] Riekel, C., M. Burghammer, and et al. *Fundamentals of non-crystalline diffraction with microfocus techniques.* Applications of Synchrotron Light to Non-Crystalline Diffraction in Materials and Life Sciences (2008).

[4] Pollack, L., M. W. Tate, and et al. *Compactness of the denatured state odf a fast-folding protein measured by submillisecond small-angle x-ray scattering.* Proc. Natl. Acad. Sci. USA, pages 10115–10117 (1999). Vol. 96.

[5] Pollack, L., M. W. Tate, and et al. *Time Resolved Collapse of a Folding Protein Observed with Small Angle X-Ray Scattering.* PRL, pages 4962–4965 (2001). Vol. 86 (21).

[6] Pfohl, T., F. Mugele, and et al. *Trends in microfluidics with complex fluids.* Chem. Phys. Chem., pages 1291–1298 (2003). Vol. 4 (12).

[7] Riekel, C. *New avenues in x-ray microbeam experiments.* Reports on Progress in Physics, pages 233–262 (2000). Vol. 63 (3).

[8] Paris, O. *From Diffraction to imaging: New avenues in studying hierarchical biological tissues with x-ray microbeams.* Biointerphases, pages FB16–FB26 (2008). Vol. 3 (2).

[9] Davies, R. J., C. Koenig, and et al. *On-axis microbeam wide- and small-angle scattering experiments of a sectioned poly(p-phenylene terephthalamide) fiber.* Appl. Phys. Lett. (2008). Vol. 92 (101903-1).

[10] Roth, S. V., M. Burghammer, and et. al. *Self-assembled gradient nanoparticle-polymer multilayers investigated by an advanced characterisation method: Microbeam Grazing Incidence X-ray Scattering.* Appl. Phys. Lett., pages 1935–1937 (2003). Vol. 82.

[11] P. Müller-Buschbaum, *et al. Creation of multi-scale stripe-like patterns in thin polymer blend films.* Europhys. Lett., **73** (1), pages 35–41 (2006). doi:10.1209/epl/i2005-10369-6.

[12] M, K., *et al. Grazing incidence small-angle X-ray scattering microtomography demonstrated on a self-ordered dried drop of nanoparticles.* Langmuir, **25** (13), pages 7241–7243 (2009).

[13] Malliaras, G. and R. Friend. *An Organic Electronics Primer.* Physics Today, **58** (5), pages 53–58 (2005). doi:10.1063/1.1995748.

[14] Du, P., *et al. Additive-Driven Phase-Selective Chemistry in Block Copolymer Thin Films: The Convergence of Top–Down and Bottom–Up Approaches.* Advanced Materials, **16** (12), pages 953–957 (2004). ISSN 1521-4095. doi:10.1002/adma.200306189.

[15] Lee, B., *et al. Structural Analysis of Block Copolymer Thin Films with Grazing Incidence Small-Angle X-ray Scattering.* Macromolecules, **38** (10), pages 4311–4323 (2005). doi: 10.1021/ma047562d.

[16] Park, S., *et al. Macroscopic 10-Terabit-per-Square-Inch Arrays from Block Copolymers with Lateral Order.* Science, **323** (5917), pages 1030–1033 (2009).

[17] Stein, G. E., *et al. Layering Transitions in Thin Films of Spherical-Domain Block Copolymers.* Macromolecules, **40** (7), pages 2453–2460 (2007). doi:10.1021/ma0625509.

[18] Sirringhaus, H., *et al. Two-dimensional charge transport in self-organized, high-mobility conjugated polymers.* Nature, **401** (6754), pages 685 – 688 (1999).

[19] Yang, H., *et al. Conducting AFM and 2D GIXD Studies on Pentacene Thin Films.* Journal of the American Chemical Society, **127** (33), pages 11542–11543 (2005). doi: 10.1021/ja052478e.

[20] Joseph Kline, R., M. D. McGehee, and M. F. Toney. *Highly oriented crystals at the buried interface in polythiophene thin-film transistors.* Nat Mater, **5** (3), pages 222 – 228 (2006).

[21] Mathijssen, S. G. J., *et al. Monolayer coverage and channel length set the mobility in self-assembled monolayer field-effect transistors.* Nat Nano, **4** (10), pages 674 – 680 (2009).

[22] Ginger, D., H. Zhang, and C. Mirkin. *The evolution of dip-pen nanolithography.* Angew Chem Int Ed Engl., **43** (1), pages 30–45 (2004).

[23] Bosworth, J. K., *et al. Control of Self-Assembly of Lithographically Patternable Block Copolymer Films.* ACS Nano, **2** (7), pages 1396–1402 (2008). doi:10.1021/nn8001505.

[24] Roth, S. V., *et al. Self-assembled gradient nanoparticle-polymer multilayers investigated by an advanced characterization method: microbeam grazing incidence x-ray scattering.* Applied Physics Letters, **82** (12), pages 1935–1937 (2003). doi:10.1063/1.1563051.

[25] Muller, A. and J. Grazul. *Optimizing the environment for sub-0.2 nm scanning transmission electron microscopy.* Journal of Electron Microscopy, **50** (3), pages 219–226 (2001). doi:10.1093/jmicro/50.3.219.

[26] Muller, D. A., *et al. Room design for high-performance electron microscopy.* Ultramicroscopy, **106** (11-12), pages 1033 – 1040 (2006). ISSN 0304-3991. doi:DOI: 10.1016/j.ultramic.2006.04.017. Proceedings of the International Workshop on Enhanced Data Generated by Electrons.

[27] Otten, A., *et al. Microfluidics of soft matter investigated by small-angle X-ray scattering.* J. Synchrotron Rad., **12**, pages 745–750 (2005).

[28] Schoeck, J., *et al. Na-Cellulose Formation in a Single Cotton Fiber Studied by Synchrotron Radiation Microdiffraction.* Biomacromolecules, **8** (2), pages 602–610 (2007). doi:10.1021/bm060844w.

[29] Graceffa, R., *et al. Synchrotron radiation microdiffraction of ballistic molten wax microdrops.* Review of Scientific Instruments, **79** (8), 086106 (2008). doi:10.1063/1.2964108.

3.6 Short pulse beamline

3.6.1 Overview

The high repetition rate, ultra-short pulses of the ERL will enable an x-ray beamline to be designed and optimized for time-resolved scattering and core-level spectroscopic studies. It will be a world-leading instrument, enabling ultrafast studies in two modes: 50 femtosecond or 2 picosecond x-ray pulses at repetition rates of $1.3\,\mathrm{GHz}$ with a time-average flux comparable to that of current third generation storage-ring-based sources. This x-ray beamline will take maximum advantage of the low emittance, the ultra-short pulses, and the high time-average spectral brightness provided by the ERL.

The proposed facility will combine ultrafast $(50 - 100\,\mathrm{fs})$ x-ray pulses with a variety of excitation mechanisms, including: short laser pulses, electrical and magnetic excitations, and coherent THz pulses tuned to specific phonon and vibrational modes to generate transient states of matter and the hard x-ray pulses from the ERL to probe the structural dynamics initiated by the excitation. The x-ray probe pulses will be produced by the (compressed) electron bunches passing through a Delta undulator, providing complete control of the polarization state of the x-ray probe. The optical pulses will be produced by optical lasers synchronized to the ERL's drive laser. The THz pulses will be produced as the (short) electron bunch passes through a dipole magnet just before the undulator, generating coherent synchrotron radiation. Since both pulses are created by the same or adjacent electron bunches, there should be little timing jitter.

The instrument design will emphasize versatility. To maximize the range of phenomena that can be studied, it will be necessary to be able to manipulate the laser pulse energy, frequency, and temporal profile. X-ray scattering will be the dominant tool for probing laser-induced changes in atomic positions, while x-ray absorption and emission spectroscopy will be used to probe changes in the electronic structure. To this end, the monochromator should provide less than 1 eV resolution for XANES/EXAFS studies and be removable or broadband for scattering/diffraction studies. All of these experiments require the union of four experimental capacities: the generation and delivery of x-ray and laser pulses to the sample, the preparation of the excited or aligned state of the sample, and the detection of the x-ray scattering pattern or of the x-ray absorption and emission spectra.

3.6.2 General motivation for a high repetition rate, ultra-short pulse instrument

For over a century, our fundamental understanding of the atomic-scale structure of materials has been advanced primarily by direct structural measurements of periodic materials using x-rays. However, matter is not static. The characteristic time for atomic rearrangements in matter is set by the characteristic vibrational period of an atom, which can be estimated to be

$$T_{\nu ib} = 2\pi(k/m)^{1/2} \simeq 1\,\mathrm{ps},$$

where we have assumed a spring constant $k = 1\,\mathrm{eV}/a^2$, spacing $a = 3\,\text{\AA}$, and mass $m = 10^{-25}\,\mathrm{kg}$. Thus, atomic rearrangements during chemical reactions, phase transitions, and responses to external stimuli are expected to occur on time scales in the 0.1 to 10 picosecond range. Thus, $50\,\mathrm{fs}$ x-ray pulses from the ERL offer the tantalizing opportunity to probe
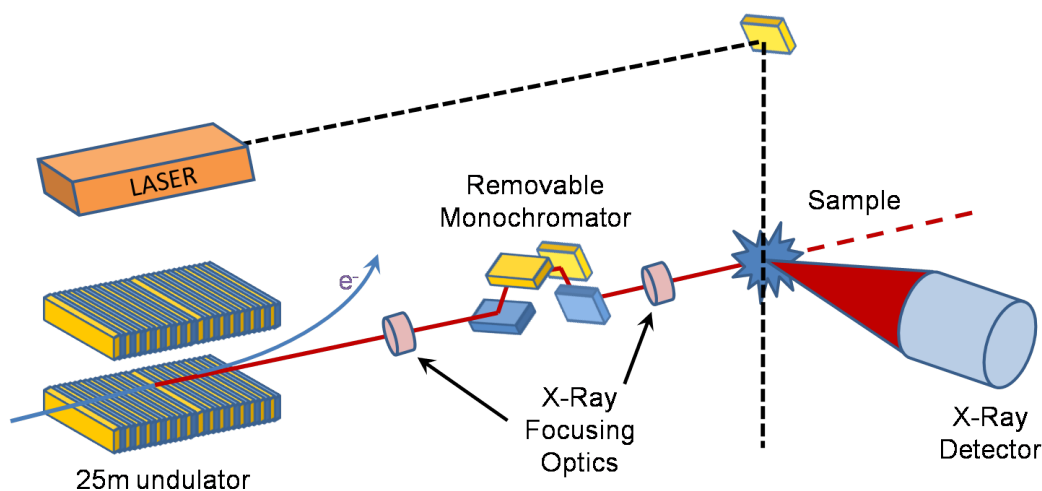
Figure 3.6.1: Conceptual layout of ultra-short pulse beamline

directly physical phenomena on the time and spatial scales relevant to the atomic, nuclear, and even electronic dynamics that govern physical, chemical, and biological processes. Ultrafast x-ray measurements provide unique measurement capabilities as x-rays can probe specific intermediate states using the distinct contrast mechanisms in resonant and non-resonant x-ray absorption and scattering.

The time scales accessible with this beamline will permit detailed spectroscopic and scattering studies of a range of materials and scientific issues including: (i) coherent control of gas phase molecules; (ii) condensed phase chemistry at interfaces and in confined geometries; (iii) chemistry in heterogeneous systems; and (iv) laser-pump XPCS studies of condensed phase dynamics.

High-repetition-rate ultrafast sources on storage rings or the ERL are complementary to free electron laser sources such as the LCLS. The ERL will excel at experiments where stability and energy tunability are essential or where multiple measurements on the same sample volume are required.

3.6.3 THz pump/hard x-ray probe studies

This beamline will be designed to include THz extraction from an optimized source location downstream of the undulator. Assuming $77\,\mathrm{pC}$/bunch, the coherent synchrotron radiation from a dipole can be much stronger than that from conventional table-top sources. The availability of intense ultrafast THz pulses will enable novel studies of materials.

The THz spectral range is associated with collective charge, spin, and lattice excitations. Thus, THz pump/hard x-ray probe studies explore the coupling between low-energy collective excitations and structure or electronic properties. In particular, the THz could be used to excite a particular low-frequency lattice mode such as those related to ferroelectricity while x-rays are used to probe the change in a lattice constant or a core-level electronic transition. A fascinating example would be to use the THz to drive the electronmagnon mode in multiferroic materials [1–4] and sense the magnetization state of various spins using element specific x-ray
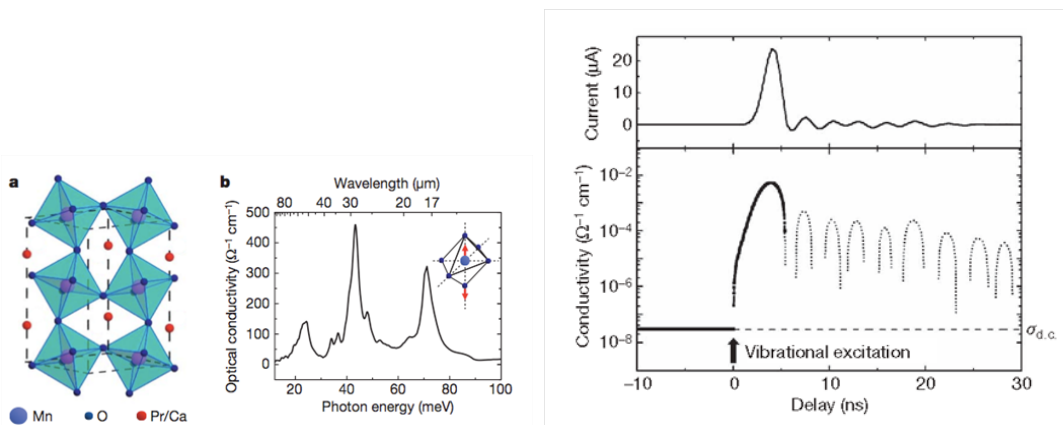
Figure 3.6.2: Time-dependent transport measurement. THz excitation ($17.5\,\mu$m,$1\,\mu$J/pulse) of the Mn-O stretching mode in $Pr_{0.7}Ca_{0.3}MnO_3$ results in a 10^3 increase in the sample current (upper panel) and a corresponding 10^5 increase in the sample conductivity (lower panel). The metastable metallic phase is both formed and relaxes within the experimental time resolution of $4\,$ns. From [6].

Circular Dichroism.

Time-resolved x-ray spectroscopy and diffraction would provide unique insight into the nature of such all-optical, phonon-mediated phase transitions. x-ray linear dichroism (XLD) measured at the Mn $L_{2,3}$ edges provides a distinct signature of orbital ordering in a related manganite [5]. Hence, tr-XLD following THz excitation of specific phonon modes would reveal directly the orbitals involved in the establishment of the metallic state as well as orbital and charge ordering. In correlated systems where the metallic state is accompanied by ferromagnetic (FM) order, time-resolved x-ray circular dichroism (tr-XMCD) can resolve the appearance of long-range FM ordering on relevant timescales.

The THz controlled metal insulator transition (MIT) in $Pr_{0.7}Ca_{0.3}MnO_3$ (PCMO) is an example of the type of experiments that would be enabled by this beamline [6]. In this study, high frequenct=y THz ($17.5\,\mu$m) pulses with an energy of $1\,\mu$J/pulse excite a specific vibrational mode: the Mn-O stretching mode of the PCMO perovskite lattice. This excitation alters the electronic bandwidth of the PCMO. The THz-driven transition is monitored by time-resolved transport measurements, which demonstrate that the sample, normally an insulator across the entire Pr/Ca composition range, undergoes a MIT in less than $4\,$ns, which was the time resolution of the experiment.

3.6.4 Bulk, interface, and confined chemistry

Chemistry occurs primarily in liquids or at the liquid solid interface. The properties of the solvent, particularly its structure and dynamics, determine the reaction mechanisms and the branching ratios. Ultimately, our ability to control chemical reactions hinges on developing a detailed understanding of the fundamental properties, in particular the transition states, of the solvent. In aqueous solutions, the important charge transfer processes take place on the 1-20 ps timescale. The aqueous hydration structure of bromine following UV excitation

has recently been studied using tr-XAS [7]. The current time-resolution available does not, however, allow observation of intermediate steps. Understanding these intermediates is crucial to understanding the role of the solvent in chemical reactivity.

Ionic liquids pose fundamental questions about the balance between weak hydrophobic interactions and intrinsic charge ordering. Almost all interfaces involving ionic liquids adopt a charge-layered structure. GISAXS and XRR studies can be combined to compare interfacial to bulk-solution structures.

3.6.5 Chemical reaction dynamics at interfaces

The vast majority of industrially and economically important chemical reactions take place in a heterogeneous environment. Supported catalysts, batteries, and fuel cells are just a few of the technologically relevant structures. Tools that visualize the correlations between structure and excited electronic states are critical for guiding the development of the theories needed for rational design and engineering of reaction conditions and optimized device structures.

Nanofocus (100 nm focal spot) will enable use of micro- and nano-electromechanical cells optimized for grazing incidence techniques. An example is the catalytic splitting of water at a Pt surface. A coplanar stripline with a middle Pt electrode about $1\,\mu$ wide submerged in water will enable the RF-structure to be tuned so that most of the electric field lines are normal to the Pt-surface. A 500 fs THz pulse, either from an Austin switch in the device or from the ERL, will travel along the strip line creating a potential gradient on the Pt-surface, shifting the effective work function and, therefore, the probability for electron transfer/tunneling through the interface barrier into the water-surface layer. Thus, the electric field strength at the surface can be used to tune the reaction rate. The grazing incidence geometry concentrates the x-ray beam at the interface, reducing background scattering and absorption.

3.6.6 tr-XRD: Complete reconstruction of unit cell dynamics

In order to completely understand the dynamics of a structure in response to a perturbation, the ideal diagnostic tool would be the ability to construct a 3D 'movie' of the atomic positions in the unit cell. This would allow us to avoid making *a priori* assumptions about the motion. Clearly, the technique requires sufficient time resolution to see the relevant dynamics. Femtosecond x-ray diffraction offers the promise of exactly this kind of measurement. A recent publication [8] reports just such a complete characterization of the unit cell dynamics of a laser-excited tellurium crystal using femtosecond x-ray diffraction. Their analysis provides a quantitative description of the unit cell dynamics without making any assumptions on the symmetry of the excited-state motion, demonstrating a large-amplitude, coherently excited, A1 mode quantitatively consistent with the predictions of a density-functional theory model.

3.6.7 Brief description of a TR-beamline

Two endstations are envisioned. First, for spectroscopic studies, a standard complement of ionization chambers, avalanche photodiodes (APDs), and fluorescence detectors would be required. A complicating factor is the need to gate detectors (or the x-ray beam) at the repetition rate of the pump lasers, which may limit the types of spectroscopy detectors used in the measurements. The second class of experiments will emphasize non-resonant scattering. A
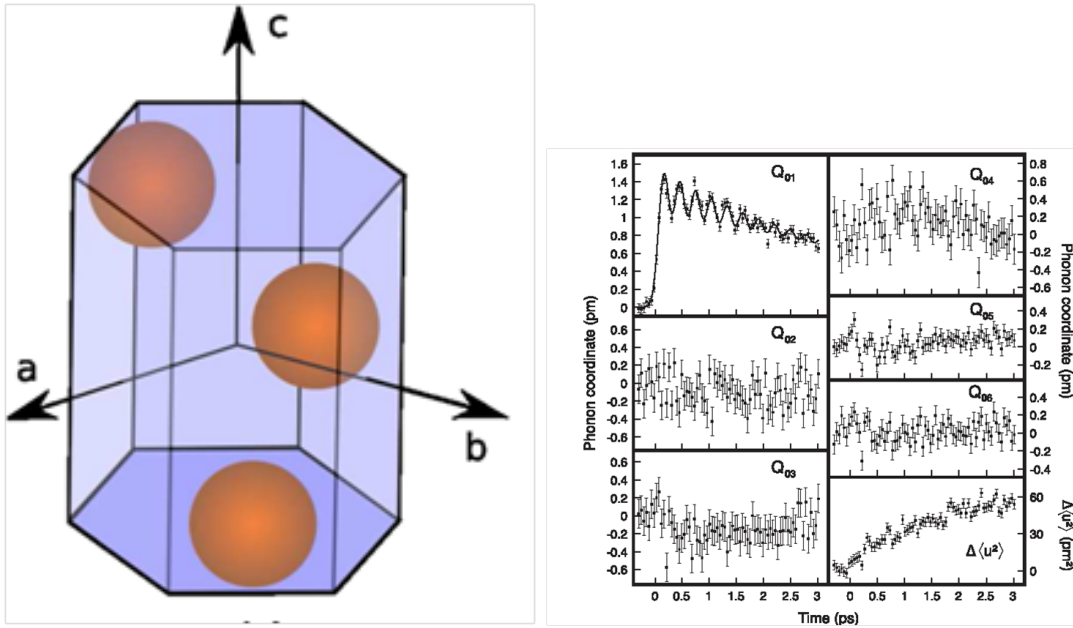
Figure 3.6.3: (Left) The hexagonal unit cell of tellurium ($a = 4 : 456\,\text{Å}$, $c = 5 : 921\,\text{Å}$), showing the three basis atoms arranged along a screw axis parallel to the c axis. With this choice of origin, the basis atoms are located at $(x, 0, 0)$, $(0, x, 1/3)$, and $(-x, -x, -1/3)$, where $x = -0.2636$ at room temperature. (Right) Phonon mode and mean-square displacement dynamics of photo-excited tellurium. From [8].

fairly standard six-circle diffractometer is envisaged. The detector complement would include APDs and PADs, which have the advantage of capturing a large segment of reciprocal space in parallel, thereby improving the efficiency of the experiment.

References

[1] Spaldin, N. A. and M. Fiebig. *Materials Science: The Renaissance of Magnetoelectric Multiferroics.* Science, pages 391–392 (2005).

[2] Pimenov, A., *et al. Possible evidence for electromagnons in multiferroic manganites.* Nat Phys, pages 97–100 (2006). Vol. 2 (2).

[3] Sushkov, A. B., *et al. Electromagnons in Multiferroic YMn2O5 and TbMn2O5.* Phys. Rev. Lett. (2007). Vol. 98 (2), 027202.

[4] Aguilar, R. V., *et al. Origin of Electromagnon Excitations in Multiferroic RMnO3.* Phys. Rev. Lett. (2009). Vol. 102 (4), 047203.

[5] D. J. Huang and W. B. Wu and G. Y. Guo and H. J. Lin and T. Y. Hou and C. F. Chang and C. T. Chen and A. Fujimori and T. Kimura and H. B. Huang and A. Tanaka and T. Jo. *Orbital Ordering in La0.5Sr1.5MnO4 Studied by Soft X-Ray Linear Dichroism.* Phys. Rev. Lett. (2009). Vol. 92 (8), 087202.

[6] Rini, M., *et al. Control of the electronic phase of a manganite by mode-selective vibrational excitation.* Nature, pages 72–74 (2007). Vol. 449 (7158).

[7] Fischer, M. K., A. Laubereau, and H. Iglev. *Femtosecond electron detachment of aqueous bromide studied by two and three pulse spectroscopy.* Physical Chemistry Chemical Physics, **11** (46), pages 10939–10944 (2009).

[8] Johnson, S. L., *et al. Full Reconstruction of a Crystal Unit Cell Structure during Coherent Femtosecond Motion.* Phys. Rev. Lett. (2009). Vol. 103 (20), 205501.

3.7 High resolution inelastic x-ray scattering beamline

Overview

The exceptionally large spectral brightness of ERL x-ray beams produced by long (e.g., 25 m, 10,000 pole) undulators, will transform the field of high resolution (meV to eV) inelastic x-ray scattering (IXS). IXS is sensitive to a variety of important electronic, magnetic, and vibrational excitations including [1, 2]: conduction electron density fluctuations (plasmons); inner-shell electronic excitations; collective vibrational modes (phonons), and the electron momentum density (by Compton scattering). Complementary experimental methods include optical Brillioun and Raman scattering, electron energy loss spectroscopy (EELS), and inelastic neutron scattering (INS). In contrast to optical probes, IXS is able to probe optically opaque systems and atomic length scale at finite momentum transfers. IXS does not require the vacuum environment or thin samples required for EELS. IXS probes electron density fluctuations with sensitivity comparable to neutrons for nuclear motions. Crystalline systems are studied with both methods, but IXS has advantages in the absence of periodicity and with small samples. For example, acoustic excitations in liquids and glasses can be studied with IXS at small momentum transfer where thermal neutron speed is a limiting factor [3], and IXS is far better for studying very small samples (e.g., in diamond anvil cells).

Uniqueness of an ERL-IXS facility

The ERL's ability to support very long undulators provides a key performance enhancement for high resolution inelastic scattering experiments, which is a spectral brightness limited technique. Equation (3.2.1) shows that the maximum number of useful poles in an undulator is limited by the fractional energy width of the electron beam. Maximizing the number of useful poles simultaneously produces the highest flux and achieves the narrowest harmonic bandwidth, so the spectral brightness of a given harmonic scales as the square of the number of poles. Clearly, the combination of small electron beam emittance and small energy width (dispersion) of an ERL is a large advantage for these experiments.

ERL electron beam emittance will be isotropic, enabling operation of a Delta undulator that easily switches x-ray polarization between horizontal, vertical, and elliptical states. Vertical polarization eliminates the $\cos^2(2\theta)$ ($2\theta =$ scattering angle) signal reduction characteristic of large horizontal IXS spectrometers. Figure 3.7.1 [1] shows flux through a 1 mm aperture at 50 m for a 20 m Delta ID with 18 mm period. The red curve is 1st harmonic flux in helical mode; black curves show tuning range for planar mode harmonics 1,3,5.

Sample experiments

Experiments illustrating the range of science enabled by an ERL-IXS beamline include new biological applications made practical by the unprecedented spectral flux and materials studies dependent on ultra-high brightness.
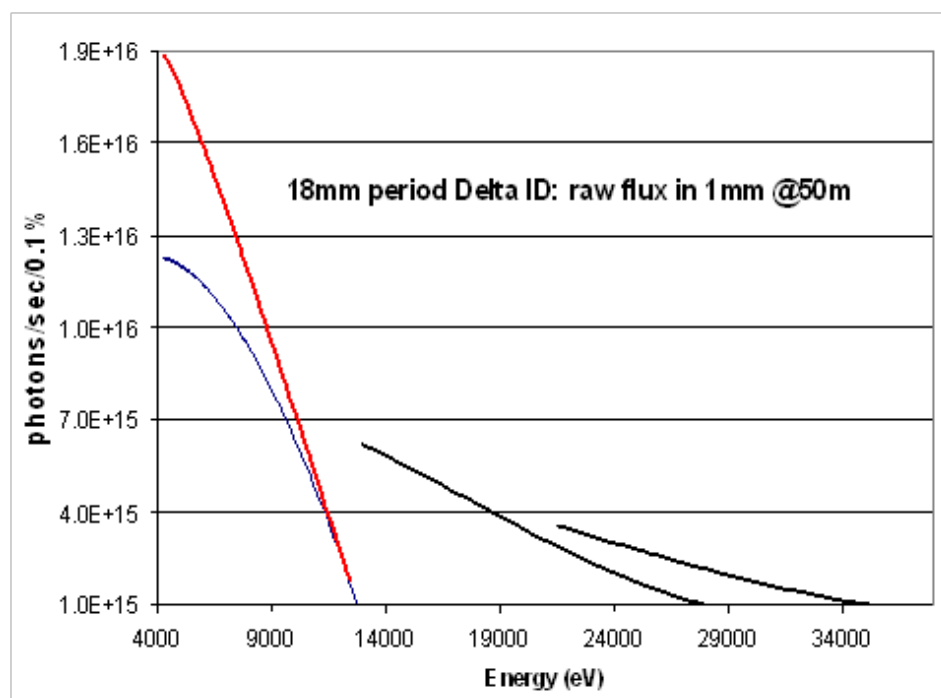
---

[1] Spectral calculations from SPECTRA8.0.8.

Figure 3.7.1: Spectral properties of Delta undulator optimized for meV applications.

Ultra-high spectral flux studies: RNA conformational dynamics

RNA has diverse biological roles. For example, 'riboswitches' are mRNA conformational switches that turn downstream genes on or off. Their recent discovery has provided strong motivation to understand RNA conformational dynamics. RNA also has great therapeutic potential as it can be engineered to carry out sequential functions: so-called 'aptameric' domains can be designed to selectively bind targets, and once bound, coupled 'catalytic' RNA domains would disrupt the bound molecule. Like proteins, RNA can be described by primary (sequence), secondary (helices) and tertiary structures (the 'fold'); however properties of its precursors (4 physically similar nucleotides as opposed to the 20 varied amino acids in proteins) make biologically active RNA structures quite similar compared to the variations in proteins. In addition, double-stranded RNA is remarkably rigid, with a persistence length on order 700 Å, far longer than helical elements in a functional RNA. For this reason, RNA structures are readily described by physical/mechanical models. To provide flexibility for a large RNA to fold to a compact functional form, short, rigid helical elements are connected by flexible single-stranded regions such as loops, hinges, or junctions. These allow the molecule to bend and twist into structures subsequently stabilized by additional chemical bonds. In this simple view, inflexible structures are connected by 'springs' that not only provide flexibility, but their relative flexibilities may dictate the order of folding.

Figure 3.7.2, from reference [4] illustrates the molecular architecture for a typical functional RNA. Since helical (double-stranded) regions are rigid on hundreds of Å length scales, non-base-paired regions provide flexibility [5]. Loops, junctions or bulges found in all functional ribozymes facilitate backbone contortions that accompany compaction and folding. The im-
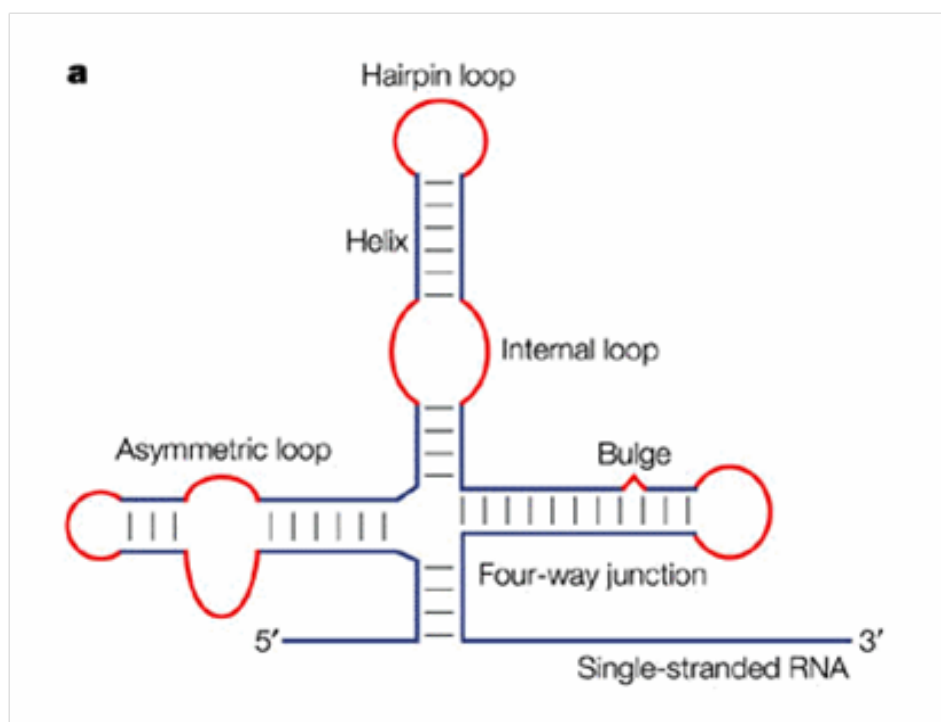
Figure 3.7.2: Molecular architecture for a typical functional RNA; from reference [4].

portance of hinges and loops to RNA folding has long been recognized; but a means to quantify and use the mechanical properties in molecular design remains elusive. X-ray scattering provides an ideal match to the length scales; loops typically span 2 - 6 base pairs or $6 - 25\,\text{Å}$. Comparing IXS spectra of rigid (unfolded) and flexible (folded or partially folded) RNA will help quantify flexibility of 'entropic springs' that connect rigid strands. Previous work suggests that persistence length (spring constant) depends on ionic strength of the surrounding solution; thus IXS spectra acquired at low and moderate ion concentration should give information about the changing flexibility.

Here, we use Sow-Hsin Chen's pioneering IXS studies of DNA in its liquid crystalline phase [6] to estimate signal, background, and radiation damage in an RNA solution inelastic scattering experiment similar to the one described above. The flux at APS 3ID was $6 \times 10^8\,\text{p/s}$ in an energy interval of $1.2\,\text{meV}$ in $200 \times 150\,\mu\text{m}^2$ @ $21.657\,\text{KeV}$, and a single analyzer-crystal collected data for 30 sec/point or 160 min/scan. With high-energy x-rays, biological samples are usually thin compared to the absorption length, μ^{-1}. Chen's samples were $6 - 10\,\text{mm}$ thick ($5 - 10\%$ absorption). For comparison, water has μ^{-1} about $1.5\,\text{mm}$ at $9.1\,\text{KeV}$ and $17.3\,\text{mm}$ at $21.75\,\text{KeV}$.

At the same energy and momentum resolution, the ERL should deliver $\sim 2 \times 10^{11}\,\text{p/s}$ (333X) and the focus could be as small as μm^2. Current analyzer-collector arrays use 4 to 12 crystals. For liquid scattering (isotropic about the zero beam direction at modest angles), analyzers could be arranged on an arc at a fixed angle. With six analyzers the DNA liquid crystal signal would increase 2000X. Scaling this result for a 1mM solution RNA sample reduces the gain to

40X. If all else were equal, comparable data would be collected in 4 min/scan.

Radiation damage: By comparing our 'pink beam' SAXS work at APS 8ID with Chen's study at APS 3ID (where no damage was observed after a 24-hour exposure) we expect the ERL radiation dose is not likely to cause damage. Two factors are important: reduced flux on the sample because bandwidth is 10^{-5} smaller, and absorption is reduced $\sim 2^3$ at higher energy [7].

These estimates based on ERL quality beams leads to the following conclusions:

- Solution IXS at biologically relevant concentrations will be feasible.

- IXS measurements currently requiring days will take hours or less.

The small spot size of the ERL beam creates additional opportunities:

- Microfluidic flow cell study of biological solutions will be possible.

- Comparing IXS solution scattering to IXS on liquid crystals, we expect a reduction in signal-to-noise for solution samples that are mainly water [2].

High spectral brightness: IXS experiments in a DAC

Knowledge of the behavior of materials at extreme conditions underpins our understanding and the modeling of bonding and structural stability. This is essential to improve the performance of current materials, and to synthesize new materials needed to address future technological applications. While structural and spectroscopic studies above 300 GPa (3 Mbars) and magnetic and superconducting studies to above 100 GPa, have revealed a wealth of remarkable phenomena in dense metallic and molecular systems, almost nothing is known about the detailed dynamics of new super-hard materials, and gases that transform into superconducting metals. Data about these phases would provide vital information on new forms of chemical bonding, on the mechanisms of phase transitions, and on elasticity, toughness and hardness of these materials.

The key limiting factor in using IXS to study dynamics in a DAC is the small sample size, $\sim 10\,\mu$m across $\sim 2\,\mu$m thick at 100 GPa, which produces extremely weak signals. The unmatched spectral brightness of undulator beams from the ERL will enable researchers to probe the dynamics of unique high-pressure phases of matter that are currently inaccessible at third-generation sources. One example is metallic superconducting oxygen. Above 10 GPa, oxygen adopts a unique structure comprising layers of parallel O_2 molecules grouped into $(O_2)_4$ clusters as indicated in Fig. 3.7.3 [8].

This arrangement is remarkably stable and persists up to 96 GPa, where there is a transition to a molecular metallic state that is superconducting below 0.6 K. Inter-cluster bonding increases with pressure, and this is expected to result in metallization via band overlap. The

---

[2] The time required for given S/N depends on total count rate and precise characterization of $S(Q,\omega)$ from water in the sample cell (for background subtraction). References [2] and [3] include scattering data from water at zero energy loss (peak of elastic signal); we scale and estimate maximum background in the solution scattering experiment ~ 1200 Hz. If the RNA signal were 2% of this, a $S/N = 5$ at the elastic peak $(5 = \sqrt{T(\sec)1200/50})$ requires $T = 52\,\sec$/pt. Collection time at fixed S/N drops as $\sim$ total counts^{-1} as energy loss increases from zero.
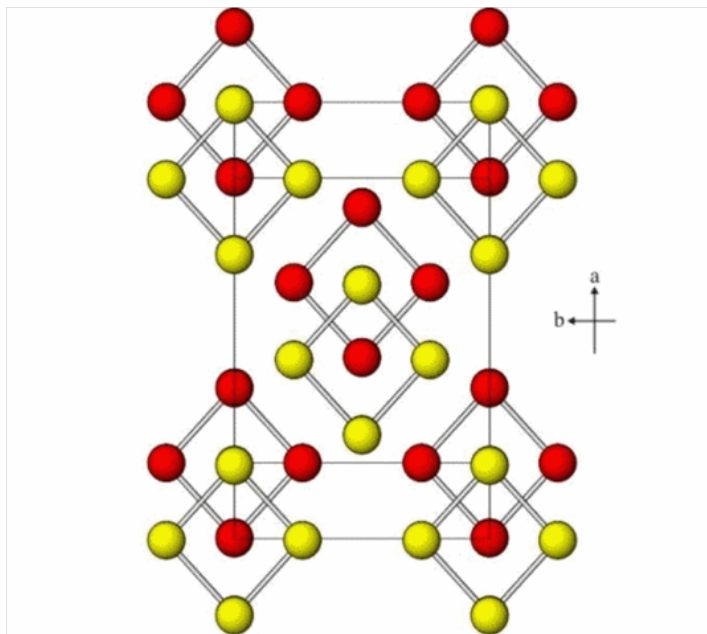
Figure 3.7.3: Structure of metallic superconducting oxygen; from reference [8].

transition to the metallic state may also involve a rearrangement and sliding of molecular layers. The $(O_2)_4$ structure has infra-red absorption that is strikingly similar to hydrogen at megabar pressure, so an understanding of bonding and dynamics in this phase is likely to provide new insight into the behavior of the most fundamental of all materials (hydrogen). X-ray Raman scattering studies, recently performed on the $(O_2)_4$-phase to 38 GPa, reveal changes in electronic structure and bonding[9]. But nothing is known about the lattice dynamics of the $(O_2)_4$-phase, nor about the transition mechanism at 96 GPa, because weakness of the IXS scattering currently precludes such a study. The ERL, with its extreme brightness and micro-focusing abilities, will overcome these limitations, enabling researchers to extend the x-ray Raman method into the metallic phase, study the phonon dynamics of the $(O_2)_4$ structure, its pressure dependence at the onset of inter-cluster bonding, and the phonon softening that may be a precursor to metallization and the onset of superconductivity. Such capabilities will revolutionize the study of exotic extreme condition phases, leading to breakthroughs in the understanding of matter in our quest for new classes of useful materials.

IXS facilites: Current state of the art

Premier facilities for IXS are listed and compared with the ERL in Tab. 3.7.1. An ERL IXS facility can potentially outperform all existing beamlines, their proposed upgrades, and new sources under construction because IXS methods take unique advantage of the ERL's long insertion devices that will produce unprecedented average spectral flux(photons/sec/unit bandwidth) and brightness [10] with reduced power on x-ray optics [3] Table 3.7.1 compares

---

[3] From Eq.17 in [11] the number of photons/sec/unit bandwidth increases with ID length. This also holds for the power/solid angle and inverse cone angle. Taken together, this implies that the ratio of harmonic peak
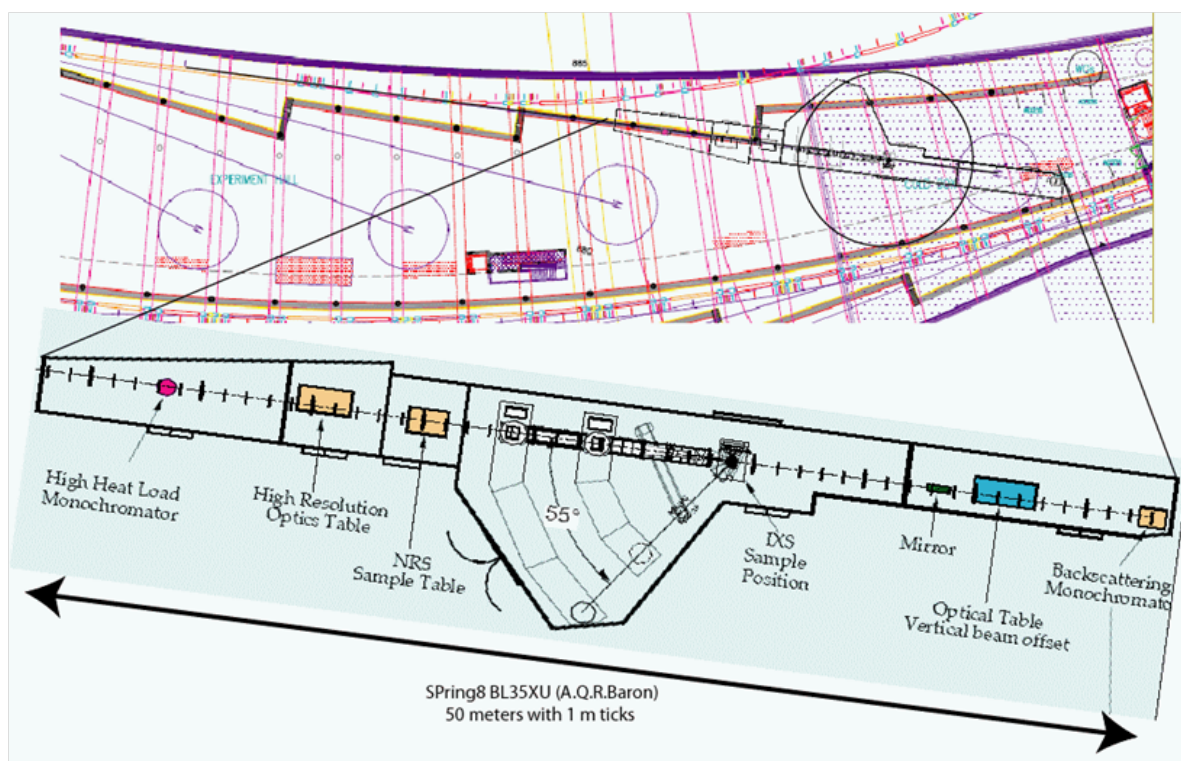
Figure 3.7.4: The Spring8 BL35XU IXS beamline (shaded) is used as a model for the ERL. It has been located on the ERL experimental floor to accept beam from a long ID straight section. A large horizontal IXS spectrometer is shown centered on a 10m radius circle. Beam from the High Heat Load Monochromator passes through the large hutch and is backscattered from the Backscattering Monochromator at the downstream end.

spectral flux from a 20m ERL Delta undulator [12] with upgrades planned for existing sources and a beamline designed for NSLS-II. A second set of numbers (in parentheses) compares spectral flux density (photons/sec/ μm^2/meV) 50m from the source. In all cases, ERL spectral flux will lead other facilities by more than one order of magnitude.

Optical design

The optics will take advantage of state-of-the-art capabilities at the time the beamline is funded. At present we plan five hutches on the experimental floor: (1) a white beam optics hutch with high-heat-load (HHL) monochromator, (2) a hutch for in-line high resolution optics, (3) a small medium resolution (2m arm) spectrometer hutch for RIXS and XES, and (4,5) two larger hutches for approximately 1 meV IXS using backscattering optics similar to present day instruments [14, 15]. This is a conservative design based on proven concepts to create leading capabilities and achieve all experimental goals discussed in this proposal. However, we

---

flux to power through a small aperture increases with ID length. We have taken advantage of this fact to optimize a Delta ID design for IXS [12], based on ERL high flux operating mode, using SPECTRA8 [13].
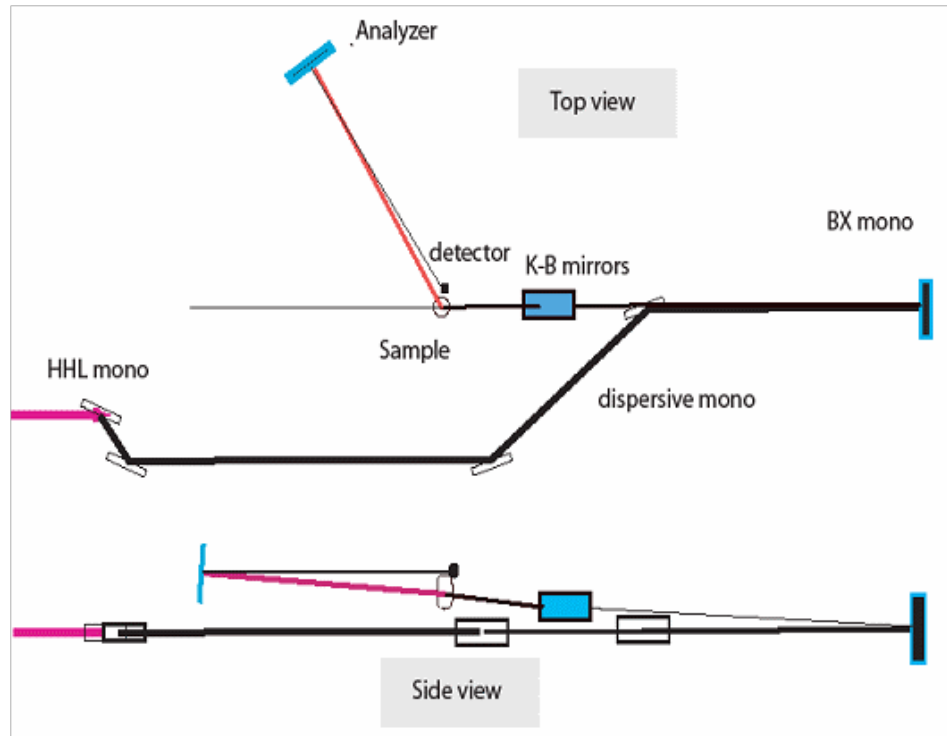
Figure 3.7.5: Illustrates the arrangement for IXS x-ray optics. At maximum K, peak flux ID 5th harmonic flux (21.75 keV) through a circular aperture @50m saturates at 1 mm diameter (20 μrad cone full width). Total power at the first optic is then 277.5 W in planar and 46.5 W in helical mode. RMS source size and divergence (vertical and horizontal) are 19 microns and $3\mu rad$.

also note that recent developments in medium, > 10 meV, resolution optics might be applied to high-resolution optics [16], and new schemes for high-resolution spectrometers might allow additional capabilities, including the possibility to accept a huge swath of momentum space with approximately meV resolution. A method to achieve meV resolution using approximately 10 keV photons has been demonstrated [17]. We are watching the development of these optics at NSLS-II, where brightness is limited above 10 keV and the long range goal is to achieve 0.1 meV resolution. While this option is unproven, we are examining it closely. For this proposal, our conservative first approximation design is similar to BL35XU of SPring-8. The other options generally have a smaller footprint on the experimental floor. In Fig. 3.7.4 we illustrate an ERL meV beamline by superimposing the Spring-8 IXS facility on to space associated with the last long ID beamline of the ERL north arc.

Facility on the ERL experimental floor

Figure 3.7.5 shows a potential beam optics layout for the downstream hutch; the following considerations have lead to this design:

1. The 1st beam optics cave houses a HHL monochromator. Due to the exceptional proper-

ties of the undulator beam, the maximum expected heat load is $< 300\,\mathrm{W}$ for essentially the entire central cone, so a liquid-nitorgen cooled HHL Si(111) monochromator should be sufficient.

2. The 2nd in-line optics hutch (see Fig. 3.7.4)will house monochromators for medium resolution, $10 - 300\,\mathrm{meV}$, appropriate for investigating electronic excitations with high to medium resolution. It will be used to prepare the beam for a spectrometer in hutch 3. Expected scan ranges for the monochromator will be at least $\sim 50\,\mathrm{eV}$, and this might be extended to $\sim 500\,\mathrm{eV}$ to allow x-ray Raman work.

3. The third hutch has a medium resolution spectrometer, with a short $2.5\,\mathrm{m}$ arm, which will take advantage of position sensitive detectors and dispersion compensation [16] to achieve resolutions between 10 and $100\,\mathrm{meV}$. The arm is slightly larger than necessary to allow greater ease in dealing with bulky sample environments. The spectrometer is expected to use the Si(nnn) family of reflections.

4. The large hutch will contain a spectrometer for studies with energy resolution 1 meV resolution or better. A large array of analyzers, 15 or more, will allow both large, solid-angle acceptance and good momentum resolution, as needed, depending on the experiment. The exact configuration and size will depend on progress achieved in optics with dispersion compensation and area detectors. The present design uses a 10m arm, sufficient to allow $0.9\,\mathrm{meV}$ resolution or better. We expect to use an analyzer with either a large 2D area or linear array. The former is advantageous for phonon studies, while the latter is better for disordered materials.

5. The last hutch houses a backscattering monochromator (BXM) that is expected to provide energy resolution between 0.3 and $4\,\mathrm{meV}$. For resolutions better than $2\,\mathrm{meV}$, this option is preferred to in-line optics because it is simpler and more efficient. At the upstream end, a pair of crystals displace the beam (to get space at the sample position) and reduce the bandwidth (and heat load) from the HHL monochromator. The 2-bounce monos in hutches 1 & 5 diffract in the horizontal to avoid polarization loss, while the BXM and analyzer crystals diffract in the vertical. A KB pair and/or refractive lenses can focus beam at the sample to a 1 micron spot.

Table 3.7.1: This table compares the expected performance for IXS, of an ERL facility, suggested upgrades of existing beamlines, and what NSLS-II is likely to deliver when mature. The uppermost section lists beam energy and monochromatopr optics required to produce given energy resolution. Subsequent (lower) sections give important beamline parameters for each facility, and their expected spectral flux and flux density.

Resolution (meV)	< 1meV	6	1.5 (1.2)	0.9 (0.6)
Silicon analyzer (hkl)	(Shvyd'ko optics)	(8 8 8)	(11 11 11)	(13 13 13)
Energy (KeV)	9.1	15.82	21.75	25.7
ERL Delta ID	93	52	35	27
λ=18mm, 20m,	$\times 10^{14} p/s/0.1\%$			
5mm gap				
1mm aperture @ 50m	(130)	(41.8)	(20.5)	(13.4)
	$\times 10^4$ p/s/meV/μ m^2			
SPring8 BL35XU		18	13	7.3
U20 4.5m	-			
0.5 $\times$ 1.5mm^2 @ 28m		(4.76)	(2.5)	(1.2)
ESRF ID28 @ 300mA.		11.2	7.2	5.4
3 Revolver IDs	-			
0.6$\times$ 1.6mm^2 @ 27m		(2.15)	(1)	(0.64)
APS Sector 30			5.7	3.9
100mA. 3 x U30 Ids	-	-		
0.4 $\times$ 2mm^2 @ 30m			(1.2)	(0.68)
NSLS-II baseline	9.95	1.69	0.07	
500mA U20 5m hi-β				-
0.6 $\times$ 1mm2 @ 30m	(6.56)	(0.64)	(0.02)	

- ERL Delta ID flux calculations assume helical mode below 12.4 keV, planar above.

- Other numbers are from AQR Baron except SPECTRA 8.0 calculations for NSLS-II based on IXS@NSLS-II Feb.2008 workshop report by Yong Cai.

- Upper number flux through aperture size at distance specified at left, Lower number - photons/sec/meV/micron^2 scaled to 50m source distance.

References

[1] Burkel, E. *Inelastic Scattering of X-rays with Very High Energy Resolution.* Springer, Berlin (1991).

[2] Schuelke, W. *Electron Dynamics by Inelastic X-ray Scattering.* Oxford Series on Synchrotron Radiation. Oxford University Press, New York (2007).

[3] Scopigno, T., *et al. Inelastic X-ray scattering and the high-frequency dynamics of disordered systems.* Physica B, **318** (4), pages 341–349 (2002).

[4] Schroeder, R., A. Barta, and K. Semrad. *Strategies for RNA folding and assembly.* Nature Reviews Molecular Cell Biology, **5** (11), pages 908–919 (2004).

[5] Schlatterer, J. C., *et al. Hinge stiffness is a barrier to RNA folding.* Journal of Molecular Biology, **379** (4), pages 859–870 (2008).

[6] Liu, Y., *et al. Inelastic X-ray scattering studies of phonons propagating along the axial direction of a DNA molecule having different counter-ion atmosphere.* Journal of Physics and Chemistry of Solids, **66** (12), pages 2235–2245 (2005).

[7] Sinn, H. *Spectroscopy with meV energy resolution.* Journal of Physics-Condensed Matter, **13** (34), pages 7525–7537 (2001).

[8] Lundegaard, L. F., *et al. Observation of an O-8 molecular lattice in the epsilon phase of solid oxygen.* Nature, **443** (7108), pages 201–204 (2006).

[9] Meng, Y., *et al. Inelastic x-ray scattering of dense solid oxygen: Evidence for intermolecular bonding.* Proceedings of the National Academy of Sciences of the United States of America, **105** (33), pages 11640–11644 (2008).

[10] Finkelstein, K. D., *et al. Energy Recovery Linac: A next generation source for inelastic X-ray scattering.* Journal of Physics and Chemistry of Solids, **66** (12), pages 2310–2312 (2005).

[11] *X-ray Data Booklet* (2001). From equ.17, pages 2-8.

[12] Temnykh, A. Technical report (2006).

[13] Tanaka, T. and H. Kitamura. *SPECTRA: a synchrotron radiation calculation code.* Journal of Synchrotron Radiation, **8** (6), pages 1221–8 (2001).

[14] Sette, F., *et al. Collective dynamics in water by high-energy resolution inelastic x-ray-scattering.* Phys. Rev. Lett., **75** (5), pages 850–853 (1995).

[15] Krisch, M. and F. Sette. Springer-Verlag, Berlin (2007).

[16] Huotari, S., *et al. Improving the performance of high-resolution X-ray spectrometers with position-sensitive pixel detectors.* Journal of Synchrotron Radiation, **12** (4), pages 467–472 (2005).

[17] Shvyd'ko, Y. V., *et al. X-Ray Bragg Diffraction in Asymmetric Backscattering Geometry.* Phys. Rev. Lett., **97** (23), page 235502 (Dec 2006). doi:10.1103/PhysRevLett.97.235502.

3.8 Nanofocus beam line

3.8.1 Overview: Transformative science with 1 to 10 nm diameter x-ray beams

Important macroscopic properties of matter are often critically dependent on the atomic-scale structure. For over a century, x-ray crystallography has been used to determine the atomic-scale structure of crystalline materials. However, in the real world, samples are not uniform, they are not isotropic, and they are not spatially homogeneous. Furthermore, the vast majority of samples are not periodic crystals. The length scale characterizing the inhomogeneity varies (see Fig. 3.8.1) but is by definition larger than the separation between atoms. Thus, x-ray beams a few nanometer in diameter range have the potential to revolutionize the study of the atomic-scale structure of real materials.

Introduction: Structure of matter at the nm scale dependent on probe size and type

Key properties of matter are often highly dependent on the local three-dimensional structure on an atomic scale. Researchers currently characterize this structure and study its relationship to physical and chemical properties with techniques based on scanning probe microscopy (SPM), near-field scanning optical microscopy (NSOM), nuclear magnetic resonance (NMR), electron microscopy (EM), and with x-rays using probe beam sizes of order 100 nm in diameter or larger. Traditional hard x-ray diffraction (crystallography) yields sub-Angstrom resolution but only for the average structure of ordered single-crystal or powder samples 100s of nm in size (or larger). Here, the constructive interference of waves scattered by many atoms arranged on planes is required to achieve this resolution. Coherent Diffraction (x-ray) Imaging (CDI) is just now breaking the ~ 16 nm resolution barrier using beam sizes that are larger than the object while removing the requirement of periodicity [1]. Standard optical probes are much larger in diameter, limited by both the opacity of samples and the small scale of the fluorescent markers employed.

On the other hand, some technologies have spatial resolution equal to the probe beam size. For instance, EM has achieved a resolution of < 1 Å on the surface or in thin samples, but has the drawback that the electron beam size is increased by scattering when passing through more than about 100 nm of material. We believe that nanoscale x-ray beams from an ERL offer the possibility to transform hard and soft x-ray science if single-atom sensitivity can be achieved. This capability does not yet currently exist.

State of the art of probe size and technique

The ability to conduct frontier x-ray science experiments is heavily dependent on the development of highly brilliant x-ray sources, x-ray optics that can make a 1 to 10 nm diameter x-ray beam, state-of-the-art x-ray detectors, and x-ray techniques. The size scale of objects to be studied ranges from microns down to the atomic scale.

The particular opportunity with the ERL machine is to push the x-ray optics to reach a 1 nm probe size and to develop the x-ray experiments that can take advantage of this capability. Storage-ring sources will be able to work on the threshold of this area, but it will take the small round ERL source to generate as many x-rays per square nanometer on a sample as typical third generation beamlines put onto a square micron of sample.
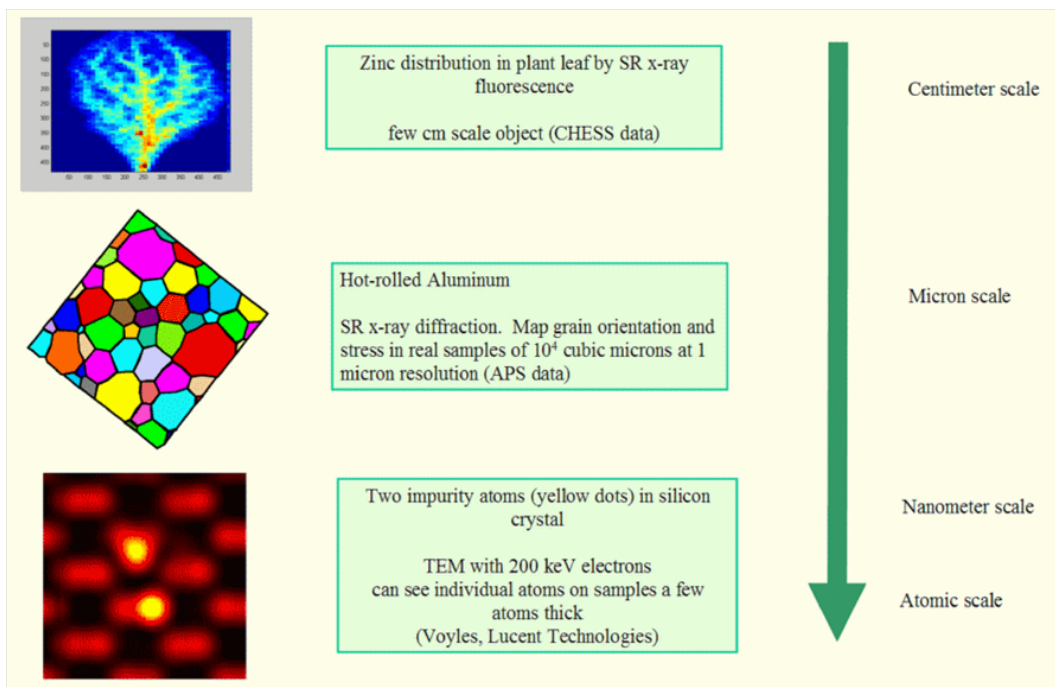
Figure 3.8.1: Size scales for micro and nanoprobe x-ray work ranges from centimeter scale down to atomic scale (transmission electron microscope image). The power of x-ray science lies in the ability to penetrate deep into the interior of objects while preserving x-ray beam size, something that is difficult to do with electron excitation.

The ERL Nanoprobe will allow the study of complex materials with spatial variation in the nanometer range, a range that is optimal for studying small nanoparticles, cells, molecules and atoms, especially those embedded in a larger context such as environmental cells, deep in layered electronic circuits, or in membranes. The primary experimental techniques for this beamline are expected to be scanning nanobeam techniques and a limited full-field capability. For the scanning beam techniques, a variety of contrast mechanisms (density, elemental composition, strain, texture, chemical state, local atomic environment, crystallographic phase, and magnetization) will allow the extraction of useful information from a real-space mapping of a sample.

Compared to current storage-ring based tools, the ERL will:

- Enable quantitative atomic-scale structure, strain, and orientation imaging on the smallest possible objects

- Increase fluorescent trace element sensitivity from the present 10^{-19} g to single atom (10^{-24} g)

- Be sensitive to chemical state via XAFS and XPS at concentrations several orders of magnitude lower than now practiced.
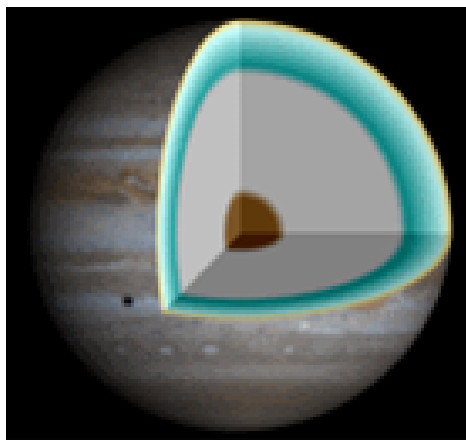
Figure 3.8.2: This cut-away illustrates a model of Jupiter's interior. "In the upper layers the atmosphere transitions to a liquid state above a thick layer of metallic hydrogen. In the center there may be a solid core of heavier elements."[2].

- Have the ability to penetrate thick layers and process environments.

Techniques to employ:

- High-resolution microscopy

- High-resolution tomography

- High-resolution anomalous and fluorescence imaging

- High-resolution diffraction imaging, coherent imaging

- spectromicroscopy (XRF, XPS, XANES, EXAFS) including single-atom imaging

With the ERL nanoprobe, we are proposing to greatly advance our capabilities to see what the local scale of atomic structure looks like on nearly an atom-by-atom basis of non-periodic samples. A few of the areas of impact are given below.

ERL performance parameters

Performance to be achieved: Intense $1 - 10\,\mathrm{nm}$ probe size (rms), $1 - 20\,\mathrm{keV}$ beam energy will allow the study of heterogeneous nanostructures, complex molecular structures and even individual atoms with intensities on the order of 10^{11} to 10^{12} x-rays/sec/nm^2 into a one nm^2 area beam at $10\,\mathrm{keV}$ behind a Si (111) monochromator.

Impact of new science enabled with the ERL

There will be a number of high-impact areas with nanobeams including the evolution of the three-dimensional structure of nano-catalysts, tracking the movement of individual ions in batteries, observing phase transitions at ultra-high pressures, study of hierarchical structure at the nanoscale level, and, for the first time, single-atom x-ray experiments.

1. **Evolution of the three-dimensional structure of nano-catalysts.** We plan to map structural changes over time during a chemical reaction in a single nano-catalyst particles where hi-z atoms such at Pt, Pd or Pb diffuse from the interior of the nanoparticle to the surface during catalysis. This will remove the averaging process over many similar but not identical particles. This should bring further clarity to the relationship between structure and function of a class of materials important to energy research and could lead to learning how to make more energy-efficient catalysts employed in industrial processes.

2. **Movement of ions in batteries.** Monitoring the movements of ions in a battery electrode during a chemical reaction while energy is expended. Most likely, we can obtain the local valence state of individual atoms undergoing a chemical reaction as well. This new type of information obtained in-situ on real materials undergoing reactions in real-world situation will directly lead to a better understanding of how these materials work and what limits their ultimate performance - all items that could result in the long term with better quality, more efficient batteries.

3. **Phase transitions at the ultra-high pressures.** With new ultra-small pressure cells based on carbon nanotubes [3–5], we believe it will be possible to study the local structure of materials undergoing high-pressure phase transitions in ultra-high-pressure cells that will exceed center of the earth pressures (350 GPa) - so that high-pressure science studies can be performed as they might exist on Jupiter (see Fig. 3.8.2), for instance. The wall thickness of a carbon nanotube is thin enough that soft as well as hard x-rays can be utilized as a probe. Thus the ERL will open a new window to the study of materials and minerals under extreme extraterrestrial conditions.

Advances to date in maximum pressure-temperature capabilities have opened new research opportunities in the studies of physics, chemistry, material sciences, and Earth-planetary sciences [6–8]. Because most high-pressure work involves the very small volumes of the diamond anvil cells, in-situ microprobe capabilities have been essential for measurements of properties of microscopic samples at ultrahigh pressures and temperatures and for the reduction of the effects of gradients across the specimens in these variables. The present state-of-the-art measurements utilize 10 micron beams at the NSLS and ~ 1 micron beams at third generation ID beam lines. The diamond anvil cell (DAC), as the most widely used device for applying extreme pressures on a material, combines two perfectly aligned gem diamond anvils to squeeze a sample loaded within the gasket hole and achieve megabar pressure. Combined with variable heating techniques, DAC techniques have been used to explore new phenomena and the resulting mechanism of a wide range of materials, including macromolecules, metal and ceramics. Results have been used to clarify the fundamental physics, design synthetic routes of novel materials, and understand the dynamics of earth's and other planetary interiors. However, the combination of hardness, yield strength and graphitization of diamond constrains the achieved pressure and temperature only below 400 GPa and 5000 K. Thus, experimental exploration above this pressure and temperature still remains blank.

Multi-wall carbon nanotubes proved being capable of filling the gap between shock wave impacted dynamic loading and DAC static compression. The extremely high Young's modulus of 1,200-1,600 GPa could allow the reaching of a $\sim$1,300 GPa pressure. The
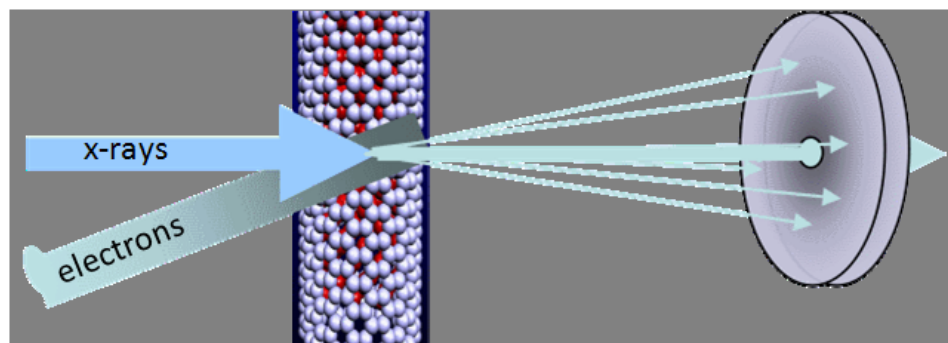
Figure 3.8.3: x-rays scattered by the sample deposit their information about local order in an x-ray area detector. Electrons from an EM microscope (at an angle) can knock out carbon atoms from a carbon nanotube. The remaining carbon bonds pull in their perimeter like a "girdle" to squeeze the contents in the carbon tube (like toothpaste) to high pressure. This new experimental arrangement offers the possibility to exceed center-of-the-earth pressures by a factor of 3 or more and also opens up the possibility of HP research with soft x-rays, not currently possible in the current thick-walled DACs.

pressure is generated upon electron beam irradiation (see Fig. 3.8.3), so the pressure-induced dynamics can be in-situ mapped out by using a wide range of x-ray absorption spectroscopies.

The nano-sized samples need highly bright synchrotron nanobeams. The ERL provides an excellent opportunity to perform this type of new generation high-pressure studies. This will also open up another new opportunity in high-pressure physics just because you can use soft x-rays for the first time. This would help to increase the interaction cross section with x-rays in a number of situations. With this particular technique and atomic resolution reached at ERL, scientists will be able to explore in-situ dynamic development of materials under significantly higher pressure than at the present time. The small samples enclosed in carbon nanotube are perfect crystal without defect, so the kinetics on how the crystal develops through a sequence of elastic, plastic, new phase and voids can be fully clarified. Results can be compared with the HRTEM observation (see Fig. 3.8.1), thus providing a calibration point for practical application.

4. **Study of hierarchical structure.** By adjusting the x-ray beam size between 100 and 1 nm in diameter, the complex structure of classes of materials from biological samples to metals can be studied [9–12] (see Fig. 3.8.4). This will be useful for detecting the presence of specific atomic elements embedded in a matrix (via x-ray fluorescence).

The rapid development of nanotechnology enables filling small volumes with a wide range of materials, including gas, liquid and solid. Therefore, this technique can be extended to perform a wide range of investigations. Just as microfludic flow cells enabled record mixing times for the folding of DNA via miniaturization, the nanoscience world could greatly benefit from this kind of opportunity. By providing smaller, ultra-high quality micro and nano beams, the ERL will be able to make a significant impact, especially for
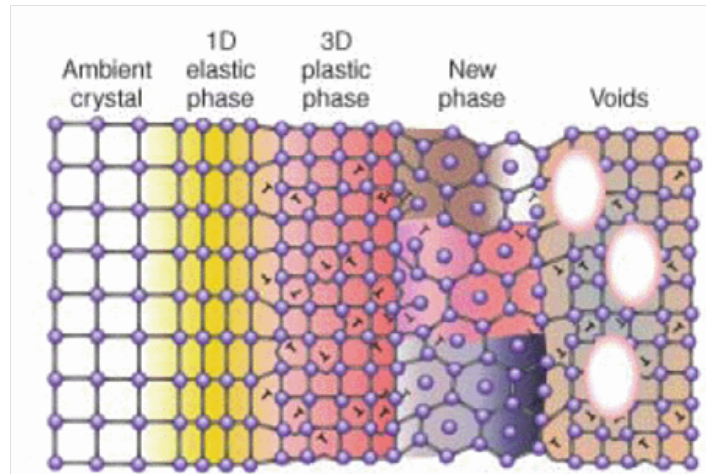
Figure 3.8.4: Nanobeams of x-rays will be able to quickly resolve mesoscopic phases of complex materials by a wide variety of x-ray scattering and spectroscopic techniques by just focusing x-rays on the phase of interest.

those situations where it can reduce measurement times from days to hours or seconds.

5. **Single-atom x-ray experiments.** For the first time, single atom x-ray experiments will be performed on a single atom or in clusters in a narrow line-width buried transistor structure. Atoms will be located using two-dimensional scanning fluorescence imaging. The electrical activity (active or inactive donor) will be determined by spatially resolved near-edge x-ray spectroscopy. This may be a useful diagnostic tool for the smallest electronic structures that require the highest dopant densities, that in turn can lead to the formation of inactive clusters when the dopant density is increased too far (see Fig. 3.8.5).

The example experiment for illustration purposes are individual Sb dopant atoms inside of very fine line-width transistors. Utilizing thin silicon structures and 200 keV electrons, inactive clusters of dopants were observed by using electron microscopy [13] .

As semiconductor line widths shrink to smaller and smaller dimension, the dopant concentration must increase until the point is reached where dopant clusters are formed and individual dopant atoms no longer contribute to further electrical activity. This is just one example of where larger scale properties are controlled by structure on a local atom-by-atom basis. We have calculated that this experiment will be repeatable with ERL x-rays (and in a threshold experiment at third generation laboratories), but $\sim 10^{11}$ to 10^{12} x-rays/s per square nanometer are needed in order to form quick fluorescent images that will be needed to carry out quick science studies. If it takes a day to collect an image or a spectra, rather than a few seconds to minutes with the ERL, then the utility of the probe will be greatly diminished.

With x-rays (instead of electrons), samples can be much thicker and in their native state, i.e. in a buried-layer transistor device, not one that has to be cut out and specially thinned. With fluorescent count rates of 10^6 x-rays/sec into a 2×pi detector, even
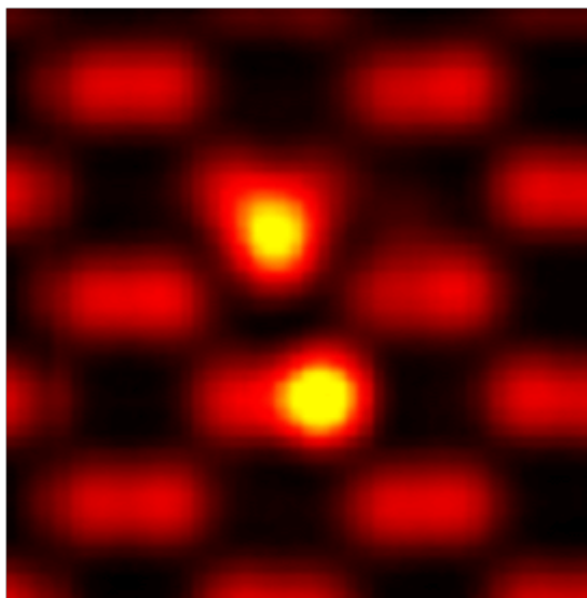
Figure 3.8.5: Two Antimony atoms (yellow dots) form an inactive cluster of dopants in a thin silicon (red dots) wafer(see [13]) as shown from this simulated image.

near-edge fluorescent spectra could be obtained that would contain information on the chemical (and thus electronic) state [14, 15].

No experiments of this type have yet been done with x-rays as the spatial resolution of hard x-ray optics has yet to reach the size of a single atom (about 1 nm diameter is needed). This is an example where the ERL nanobeams will be transformational to the frontiers of nanoscience.

3.8.2 Optical design

Micro-focused x-ray beams 0.3 to 1 micron in size have been one of the real success stories of 3rd generation synchrotron x-ray machines such as the APS, ESRF, and SPring-8 [16]. One of the limitations of storage rings, though, is that the horizontal size of beams is much larger that the vertical size. To achieve the highest spatial resolution, the most useful beams for nanobeam experimentation are round in shape. The ERL will naturally produce round beams with unfocused rms sizes of 3 - 11 microns in diameter.

A conceptual design is illustrated in Fig. 3.8.6 The source would be a $2 - 5$ m long undulator operating in a low beta drift region. The first focusing element is placed after collimating slits and outside of the shield wall at roughly the 1:1 position. As shown in Fig. 3.8.7 and Fig. 3.8.8, these collimating slits can eliminate a large component of the power in the 1/gamma cone while still passing the entire cone of the undulator's 1st harmonic. For the best focusing, a cryogenic monochromator would then follow. Final focusing would be performed in the experimental station just before the sample.

Preliminary calculations indicate that, with suitable brilliance-preserving optics, the ERL could provide focused beams down to 1 nanometer in size and fluxes of 10^{11} to 10^{12} x-
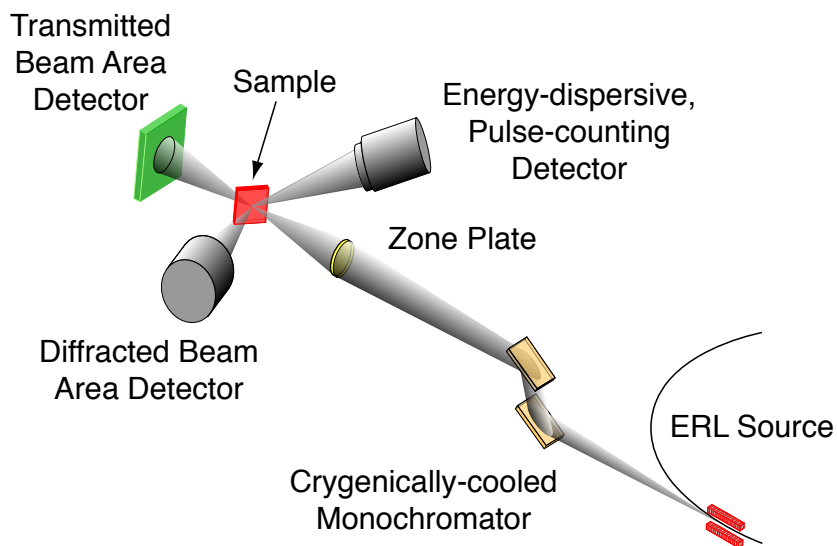
2221004-003

Figure 3.8.6: Intense 1-10 nm probe size (rms), 1-20 keV x-ray beam allows study of nanostructures and molecules, quantitative imaging of atomic-scale structure, strain and orientation, increased fluorescent trace element sensitivity from present 10^{-19} g to single atom (10^{-24} g), sensitivity to chemical state via XAFS at ultra-low concentrations, and the ability to penetrate thick layers or process gas environments.

rays/sec/nm^2 depending on bandwidth and type of x-ray optics used. The advantage is that the ERL source will provide nearly as many x-rays/per second to $1\,\text{nm}^2$ area as many third generation beam lines provide to $1\,\mu\text{m}^2$ area thus making possible many more time-resolved studies on small samples.

The main challenge will be to provide x-ray optics that are capable of making such small beams. We presently don't have optics that can reach this size scale, but are factors of 10 to 20 away with current technologies. Candidate optics for this energy regime includes Laue lenses, refractive optics, zone plates, KB and multilayer mirrors.
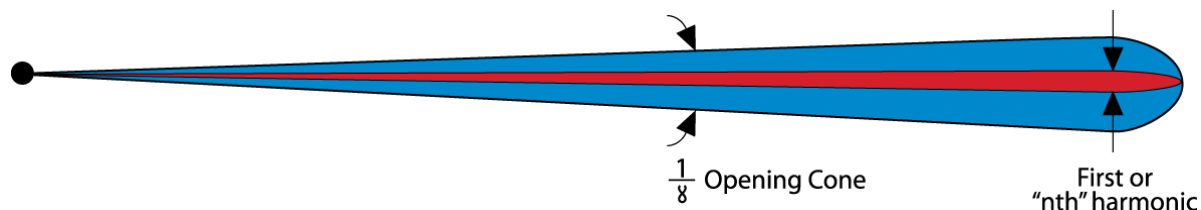
Figure 3.8.7: An x-ray undulator emits its x-ray power into an opening cone (blue) of $1/\gamma$. The first harmonic opening cone is much smaller in size (red) at 3% to 6% of the larger cone diameter for a 2 cm period undulator of 25 meter or 5 meter length on first harmonic
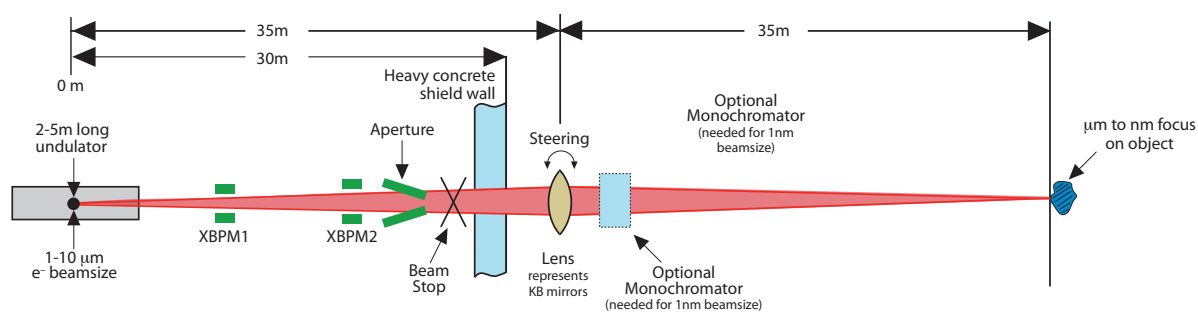

Figure 3.8.8: Conceptional design for a nanofocus beamline. A 2 to 5 m long delta undulator is the source. An aperture passes only the core of the first harmonic to the focusing mirror. A cryogenic monochromator is necessary for the highest demagnifications provided by additional optics (not shown) in the experimental station.

References

[1] Abbey, B., *et al. Keyhole coherent diffractive imaging.* Nature Physics, **4**, pages 394 – 398 (2008).

[2] *Taken from R.J. Hall (NASA).* http://en.wikipedia.org/wiki/File:Jupiter_interior.png.

[3] Wang, Z. and Y. Zhao. *High-Pressure Microscopy.* SCIENCE, **312** (5777), pages 1149–1150 (2006).

[4] Sun, L., *et al. Carbon Nanotubes as High-Pressure Cylinders and Nanoextruders.* SCIENCE, **312** (5777), pages 1199–1202 (2006).

[5] Terrones, M. *Science and Technology of the twenty-first century: Synthesis, Properties, and Applications of Carbon Nanotubes.* Annual Review of Materials Research, **33** (1), pages 419–501 (2003). doi:10.1146/annurev.matsci.33.012802.100255.

[6] Yoo, C. S., *et al. Phase Diagram of Iron by in Situ X-ray Diffraction: Implications for Earth's Core.* SCIENCE, **312** (5777), pages 1473–1475 (1995).

[7] Brown, J. M. and R. M. Queen. *Phase-transitions, Gruneisen-parameter, and elasticity for shocked iron between 77-GPa and 400-GPa.* Journal of Geophysical Research-Solid Earth and Planets, **91**, pages 7485–7494 (1986).

[8] Tsang, S. C., *et al. A simple chemical method of opening and filling carbon nanotubes.* Nature, **372**, pages 159 – 162 (2002).

[9] Riekel, C. and R. J. Davies. *Applications of synchrotron radiation micro-focus techniques to the study of polymer and biopolymer fibers.* Current Opinion in Colloid & Interface Science, **9** (6), pages 396 – 403 (2005). ISSN 1359-0294. doi:DOI:10.1016/j.cocis.2004.10.004.

[10] Riekel, C., M. Burghammer, and G. Schertler. *Protein crystallography microdiffraction.* Current Opinion in Structural Biology, **15** (5), pages 556 – 562 (2005). ISSN 0959-440X. doi:DOI:10.1016/j.sbi.2005.08.013.

[11] Roth, S. V., *et al. Self-assembled gradient nanoparticle-polymer multilayers investigated by an advanced characterization method: microbeam grazing incidence x-ray scattering.* Applied Physics Letters, **82** (12), pages 1935–1937 (2003). doi:10.1063/1.1563051.

[12] Riekel, C., M. Burghammer, and M. Muller. *Microbeam small-angle scattering experiments and their combination with microdiffraction.* Journal of Applied Crystallography, **33(1)**, pages 421–423 (2000).

[13] Voyles, P. M., *et al. Atomic-scale imaging of individual dopant atoms and clusters in highly n-type bulk Si.* Nature, **416** (6883), pages 826–829 (2002).

[14] Bilderback, D. H. and R. Huang. *Are Atom-sized X-ray Experiments Possible?* AIP Conference Proceedings, **705** (1), pages 1271–1274 (2004).

[15] Banerjee, S., D. Bilderback, and R. Huang. *Feasibility of Single-Atom X-ray Fluorescence Imaging from an Energy Recovery Linac Source of Synchrotron Radiation* (2002).

[16] Riekel, C. *New avenues in x-ray microbeam experiments.* Reports on Progress in Physics, **63**, pages 233–262 (2000).